

# SIMULATIONS OF UN-EQUAL BINARY COLLISIONS EMBEDDED IN A TURBULENT GAS CLOUD FAR AWAY OF A MASSIVE GRAVITATIONAL CENTER\*

Guillermo Arreaga-García<sup>1</sup>

*Draft version: March 24, 2024*

## RESUMEN

Simulamos el colapso de una nube turbulenta de gas usando el código basado en partículas Gadget2. Escogemos dos subnubes, formadas por aquellas partículas localizadas alrededor de los centros  $\vec{r}_L$  and  $\vec{r}_R$  y entre de los radios  $r_L$  and  $r_R$ , respectivamente. Una velocidad traslacional  $\vec{v}_L$  and  $\vec{v}_R$  se agrega, tal que las subnubes se mueven una hacia la otra para chocar. El radio y la velocidad pre-colision de las subnubes se escogen desiguales y tanto colisiones frontales como oblicuas se consideran. Las simulaciones son todas calibradas para tener la misma masa total y la razón de energía inicial  $\alpha = 0.16$ , la cual se define como la razón de la energía térmica a la energía gravitacional. Comparamos modelos de baja- $\beta$  con modelos de alta- $\beta$ , en donde  $\beta$  se define como la razón de la energía cinética a la energía gravitacional. Finalmente, consideramos que la nube turbulenta esta bajo la influencia gravitacional de un objeto localizado suficientemente lejos, con el propósito de aproximar los efectos de marea por medio de una velocidad azimutal  $V_{\text{cir}}$  agregada a las partículas de la nube adicionalmente a las velocidades traslacional y turbulenta mencionadas arriba. Comparamos un modelo de baja- $V_{\text{cir}}$  con uno de alta- $V_{\text{cir}}$ .

## ABSTRACT

We simulate the collapse of a turbulent gas cloud with the particle-based code Gadget2. We choose two sub-clouds, formed by those particles located around the centers  $\vec{r}_L$  and  $\vec{r}_R$  and within the radii  $r_L$  and  $r_R$ , respectively. A translational velocity  $\vec{v}_L$  or  $\vec{v}_R$  is added, so that the sub-clouds move towards each other to collide. The radius and pre-collision velocity of the sub-clouds are chosen to be un-equal, and both head-on and oblique collisions are considered. The simulations are all calibrated to have the same total mass and the initial energy ratio  $\alpha = 0.16$ , which is defined as the ratio of thermal energy to gravitational energy. We compare low- $\beta$  models to a high- $\beta$  models,

---

<sup>1</sup>Departamento de Investigación en Física

Universidad de Sonora. MEXICO.

where  $\beta$  is defined as the ratio of kinetic energy to gravitational energy. Finally, we consider the turbulent cloud to be under the gravitational influence of an object located far enough, in order to approximate the tidal effects by means of an azimuthal velocity  $V_{\text{cir}}$  added to the cloud particles in addition to the translational and turbulent velocities mentioned above. We compare a low- $V_{\text{cir}}$  model with a high- $V_{\text{cir}}$  one.

*Key Words:* –stars: formation — –physical processes: gravitational collapse; hydrodynamics — –methods: numerical

## 1. INTRODUCTION

There is ample observational evidence of the occurrence of cloud-cloud collisions, see Testi et al. (2000), Churchwell et al. (2006), Furukawa et al. (2009), Torii et al. (2011), Takahira et al. (2014) and Yamada et al. (2021). Regions such as RCW49, Westerlund2, and NGC 3603 are examples of cloud-cloud collisions. Collision between clouds are widely expected, because clouds moving at random directions have been observed in the plane of the Milky Way, see Roslowky et al. (2003) and Bolatto et al. (2008). As a star formation mechanism, some observations indicate that cloud-cloud collisions are the external agent to trigger the initial gas condensation at the interface of the colliding clouds. This star formation mechanism seems to be a very important step to explain the formation of high-mass stars and clusters of stars. For low-mass stars, the most relevant mechanism of formation seems to be the gravitational collapse of cloud cores, that is induced by an internal agent, such as the expansion of HII regions, see Scoville et al. (1986).

The G0.253 + 0.016 molecular cloud, which is also called the Brick, has attracted a lot of attention and is believed to be formed by a cloud-cloud collision. This cloud is a massive ( $\approx 10^5 M_{\odot}$ ) and compact 3 pc, cloud in the Central Molecular Zone of the Milky Way (CMZ). The Brick can be considered to be a possible progenitor cloud of a young massive cluster (YMC) of stars; that is, the Brick represents the initial conditions out of which high-mass proto-stars can be formed through gravitational collapse, see Petkova et al. (2006).

Longmore et al. (2012) presented deep, multiple-filter, near-IR observations of the Brick, to ascertain its dynamical state. Longmore et al. (2012) noted that large-scale emission from shocked-gas was detected toward the Brick, which indicates that this cloud could have been formed by the convergence of large-scale flows of gas or by a cloud-cloud collision.

Using ALMA line emission observations of sulfur monoxide, Higuchi et al. (2014) compared the filamentary structures observed in the cloud G0.253+0.016 with a cloud collision model.

Consequently, the shell structure was obtained theoretically which is similar to that shell-like structure observed in the G0.253+0.016 cloud. The model proposed by Higuchi et al. (2014) considered that the giant G0.253+0.016 molecular cloud may have formed due to a cloud collision between two un-equal clouds. The small cloud has a radius of 1.5 pc and a mass of  $0.5 \times 10^5 M_{\odot}$ ; the larger cloud, has a radius of 3 pc and a mass of  $2 \times 10^5 M_{\odot}$ . Their approaching pre-collision velocity is within a from 30 to 60 km/s.

Using the Combined Array for Research in Millimeter-wave Astronomy (CARMA), Kauffmann et al. (2013) presented high-resolution interferometric molecular line and dust emission maps for the G0.253+0.016 cloud. Kauffmann et al. (2013) estimated the virial parameter of the the G0.253+0.016 cloud, which yields a value of  $\alpha_{\text{vir}} < 0.8$ . In addition, Rathborne et al. (2015) used ALMA observations of the Brick to investigate its physical conditions.

Many surveys have reported the physical conditions of gas structures of the ISM, that are on the verge of collapse, see for instance, Caselli et al. (2002) and Jijina et al. (1999). The dimensionless ratios  $\alpha$  and  $\beta$ , which are defined as the ratio of thermal energy to gravitational energy and the ratio of kinetic energy to gravitational energy, respectively- are very useful to characterize the physical state of these gas structures. Observations seem to favor the statistical occurrence of low- $\beta$  clumps. However, recent observations have found a gas cloud with a high value of  $\beta$ , see for example Jackson et al. (2018). In addition, for clouds in the CMZ, the gas is observed to be highly turbulent, with high non-thermal line-widths in the range from 20 to 50 km/s. Consequently, considering an isothermal sound speed within the range from 0.3 to 0.6 km/s for gas temperatures from 30 to 100 K, the typical Mach numbers are in the range from 10 to 60, which is a highly-supersonic turbulence, see Bally et al. (1998) and Mills (2017).

From the theoretical side, a lot of simulations that aim to study a cloud-cloud collision process have appeared in the last three decades, for instance, Hausman (1978), Lattanzio et al. (1985), Kimura and Tosa (1996), Klein and Woods (1998) and Marinho and Lepine (2000). However, these early simulations were done with low resolution. Simulations with much better resolution were done more recently by Burkert and Alves (2009) and Anathpindika (2009a). Colliding gas structures starting from hydrodynamical equilibrium were considered by Kitsionas and Whitworth (2007) and Anathpindika (2009b). Anathpindika (2010) considered collisions between un-equal gas structures. Gomez et al. (2007) and Vazquez-Semane et al. (2007) and other authors, studied the generation of turbulence at the shock front of head-on collisions.

Lis and Menten (1998) proposed a model that was based on a cloud-cloud collision that

aimed to explain far-infrared continuum emission observations of the G0.253+0.016 molecular cloud. The simulation presented by Habe and Ohta (1992) assumed that the mass ratio of the non-identical colliding clouds is 1:4 and the radius ratio is 1:2.

Dale et al. (2019) and Kruijssen et al. (2019) have proposed hydrodynamical simulations of a gas cloud orbiting in the gravitational potential of the CMZ, in the radial range from 1 to 300 pc. In these simulations, each SPH particle has been given an additional external force to take the external potential of the CMZ into account.

Anathpindika (2010) studied a head-on collision between two clouds of different sizes: one cloud was modeled as a Bonnor-Ebert sphere and the second cloud was modeled as a uniform density sphere. The cloud's pre-collision translation velocities are also un-equal: one moves at 10 km/s while the second cloud moves at -15 km/s. The formation of a bow-shock is the main outcome of these simulations. The bow-shock continues collapsing, so that the models showed a lot of fragmentation while other models with slow collision velocities showed no sign of fragmentation. In addition, the author noted that this behavior (whether or not fragmentation is presented) also depends on the simulation resolution.

In this paper we aim to study the collision process of several un-equal sub-clouds, which are initially embedded within a parent turbulent cloud. The set up of this paper is similar to the physical conditions mentioned by Anathpindika (2010), Higuchi et al. (2014) and Kauffmann et al. (2013), so that the system of interest resembles the Brick. In addition, we want to see what role the initial turbulence of the cloud can have on the overall collision process. While Anathpindika (2010) and other authors have considered two separate clouds that collide, we emphasize that in this paper that the initial cloud entirely contains the two sub-clouds that collide. We consider both kinds of clouds to simulate: low and high  $\beta$  turbulent models, so that  $\beta = 0.5$  or  $\beta = 50$ . In both cases, the cloud will collapse once the initial turbulence has been dissipated. It has been shown by Arreaga (2018) that the  $\beta$  ratio can reach very high values, and yet the simulations of these clouds show that they still collapse globally.

The models considered in this paper are clearly incomplete given that they do not take into account the environment of the cloud, so that the models are taken as isolated systems, which is a common practice in numerical simulations of cloud collapse and evolution. In the case of the Brick, or in general of a cloud located in the CMZ, a tidal force will be exerted upon the clouds from a massive central object, see Molinari et al. (2011).

For this reason, we introduce an approximate model to mimic the gravitational influence

of a central massive object on the cloud, in addition to the collision process described earlier. In this approximate model, an additional velocity is added to each SPH particle of the cloud, so that this velocity is directly related to the escape velocity induced by the massive central object on the cloud. The result obtained with this simple model has allowed us to conclude that the collapse of the cloud is accelerated by the presence of the external object, as was already pointed out by Dale et al. (2019) and Kruijssen et al. (2019), using a more complete model.

It must be emphasized that this simple approximate model produces a central condensation during the very early evolution of the cloud, which is decisive in the subsequent evolution. The results obtained from these simulations are in agreement with observations (Hillenbrand and Hartmann (1998)) and simulations (Kirk et al. (2014)), which indicate that the most massive member of a star cluster is always located in the center of the cluster.

It must be noted that the gas particles of all the models include three types of velocities, which are the turbulent velocity spectrum, the translational velocity and the azimuthal velocity, all of them are given as initial conditions of the SPH particles. The particles are then allowed to evolve as gas described by the Navier-Stokes hydrodynamic equations under the influence of their own gravitational interaction.

The outline of this paper is as follows. In Section 2 we describe the initial cloud, within which all the collision models will take place. The initial conditions given to the simulation particles are explained in Sections 2.1 and 2.2. We define the azimuthal velocity in Section 2.3. Then, in Section 2.4 we give the details of the collision geometry and define the models to be studied. We describe the GADGET2 code, the resolution of the simulations and the equation of state in Sections 2.6, 2.7 and 2.8, respectively. In Section 3, we describe the most important features of the time evolution of our simulations by means of two-dimensional ( $2D$ ) and three-dimensional ( $3D$ ) plots. A dynamical characterization of the simulation outcomes is undertaken in Section 4. Finally, in Sections 5 and 6 we discuss the relevance of our results in view of those reported by previous papers and we make some concluding remarks.

## 2. THE PHYSICAL SYSTEM AND COMPUTATIONAL CONSIDERATIONS

The gas cloud that is considered in this paper is a uniform sphere with a radius of  $R_0 = 3.0$  pc and a mass of  $M_0 = 1.0 \times 10^5 M_\odot$ . The average density and the free-fall time of this cloud are  $\rho_0 = 5.9 \times 10^{-20}$  g cm $^{-3}$  and  $t_{ff} = 8.64 \times 10^{12}$  s or 0.27 Myr ( $2.7 \times 10^5$  yr), respectively. The values of  $R_0$  and  $M_0$  have been taken from Kauffmann et al. (2013) and Higuchi et al. (2014),

to draw comparisons with their models of the Brick. The number density of the cloud considered here is  $n_0 = 15352$  particles per  $\text{cm}^3$ , in which a mean molecular weight of 2.4 for the hydrogen molecule is assumed. Therefore, its mean mass is  $3.9 \times 10^{-24}$  g.

It should be emphasized that these physical properties of density, mass and radius are typical of the gas structures so-called "clumps" in the cloud classification framework of Jijina et al. (1999) and Bergin et al. (2007) of the ISM, with a number density within the range  $10^3 - 10^4 \text{ cm}^3$ . With respect to the mass, the gas structure of this paper would better correspond to a "cloud", because the typical mass of clouds is within the range  $10^3 - 10^4 M_\odot$  while that of the clumps is in the range  $50 - 500 M_\odot$ .

We therefore use the term cloud to refer to the gas structure considered here, although it is clearly much denser than a typical cloud. For a cloud structure near the CMZ, the physical properties are observed to be more extreme, so that the density number and the temperature are in general higher than the clouds of ISM in the galactic disc, see Longmore et al. (2013).

## 2.1. *The initial conditions of the simulation particles*

### 2.1.1. *The initial positions*

The gas particles are initially located in a simulation volume, which is divided into small cubic elements, with a volume given by  $\Delta x \Delta y \Delta z$ . A gas particle is placed at the center of each cubic element. Next, each particle is displaced a distance of the order  $\Delta/4.0$  in a random spatial direction within each cubic element. The total number of particles is 13,366,240. Therefore, the mass of a simulation particle is given by  $m_p = 7.48 \times 10^{-3} M_\odot$ .

### 2.1.2. *The initial turbulent velocity spectrum*

To generate the turbulent velocity spectrum, we set up a mesh with a side length equal to 2 times the cloud radius,  $L_0 = 2 R_0$ , so that the size of each grid element of this mesh is  $\delta = L_0/N_g$  and the mesh partition is determined by  $N_g = 64$ . In Fourier space, the partition is given by  $\delta K = 1/L_0$ , so that each wave-number vector  $\vec{K}$  has the components  $K_x = i_x \delta K$ ,  $K_y = i_y \delta K$  and  $K_z = i_z \delta K$ , where the indices  $i_x, i_y, i_z$  in Eq.1 take integer values in the range  $[-N_g/2, N_g/2]$  to cover all of the mesh.

A velocity vector  $\vec{v}(\vec{r}) = (v_x, v_y, v_z)$  must be assigned for a SPH particle located at position  $\vec{r} = (x, y, z)$ , which is given by

$$\vec{v}(\vec{r}) \approx \Sigma_{i_x, i_y, i_z} \left| \vec{K} \right|^{\frac{-n-2}{2}} \vec{K} \sin \left( \vec{K} \cdot \vec{r} + \Phi_K \right) \quad (1)$$

where  $n$  is the spectral index. It must be noted that this kind of turbulent velocity spectrum is known as a curl-free (CF) type. A method to obtain a divergence-free (DF) type of turbulence spectrum has been shown in Dobbs et al. (2005). Arreaga (2017) examined the effects on the collapse of cores due to variation of the number and size of the Fourier modes, for each turbulence type, whether divergence-free or curl-free. Arreaga (2017) demonstrated that the results of the core collapse are not substantially different. Arreaga (2018) presented simulations in which the velocity vector given to each SPH particle was formed by a combination of the two types of turbulent spectra  $\vec{v} = \frac{1}{2}\vec{v}_{DF} + \frac{1}{2}\vec{v}_{CF}$ .

The initial power of the velocity field, for both types of turbulence is given by:

$$P(\vec{K}) = \langle \left| v(\vec{K}) \right|^2 \rangle = \left| \vec{K} \right|^{-n} \quad (2)$$

The spectral index has been fixed in our simulations to the value  $n = -1$  and thus we will have  $P \approx K$  and  $v^2 \approx K^{-1}$ . Other authors have used other values of the spectral index, for instance  $n = 2$ , so that their power and velocity go as  $P \approx K^{-2}$  and  $v^2 \approx K^{-2}$ , respectively, see Dobbs et al. (2005).

Finally, the level of turbulence can be adjusted by introducing a multiplicative constant in front of the right-hand side of Eq. 1, whose value is fixed, as we explain it in the next Section 2.2. Later, we will show that the velocity spectrum that is proposed in this Section 2.1.2 has some of the well-known characteristics of turbulence, see Section 5.1.

## 2.2. Initial energies

In a particle-based simulation, the thermal, kinetic and gravitational energies are given by

$$\begin{aligned} E_{\text{ther}} &= \frac{3}{2} \sum_i m_i \frac{P_i}{\rho_i} \\ E_{\text{kin}} &= \frac{1}{2} \sum_i m_i v_i^2, \\ E_{\text{grav}} &= \frac{1}{2} \sum_i m_i \Phi_i \end{aligned} \quad (3)$$

where  $P_i$  is the pressure and  $\Phi_i$  is the gravitational potential at the location of particle  $i$ , with velocity  $v_i$  and mass  $m_i$ . It should be emphasized that all of the SPH particles of a simulation must be used in the summation of Eq. 3.

Let  $\alpha$  be defined as the ratio of the thermal energy to the gravitational energy and let  $\beta$  be the ratio of the kinetic energy to the gravitational energy, so that

$$\alpha \equiv \frac{E_{ther}}{|E_{grav}|} \quad (4)$$

and

$$\beta \equiv \frac{E_{kin}}{|E_{grav}|}. \quad (5)$$

The value of the speed of sound  $c_0$  has been fixed at 225,000 cm/s, so that the initial turbulent cloud has the  $\alpha_0$  ratio given by 0.16, for all the collision models. The multiplicative constant mentioned in Section 2.1.2 has been adjusted so that the initial turbulent cloud has a  $\beta_0$  ratio given by 0.5.<sup>2</sup> Higuchi et al. (2014) presented line emission observations of the Brick using the Atacama Large Millimeter/Submillimeter Array and considered values of  $\beta_0 = 0.1$  and  $\alpha_0 = 0.02$  taken into account a cloud mass of  $2 \times 10^5 M_\odot$ , radius of 2.8 pc, a temperature of 20 K and a one-dimensional velocity dispersion of 4 km/s.

The virial parameter is very useful when characterizing the physical state of a gas structure, which is defined observationally by

$$\beta_{vir} \equiv \frac{5 \sigma_{1D}^2 R}{G M} \quad (6)$$

where  $G$  is Newton's gravitational constant,  $M$  and  $R$  are the mass and radius of the gas structure, and  $\sigma_{1D}$  is the intrinsic one-dimensional velocity dispersion of the hydrogen molecule. Assuming isotropic motions, a 3D velocity dispersion can be simply related by  $\sigma_{3D} = \sqrt{3} \sigma_{1D}$ . It should be noted that a gas structure in virial equilibrium would have  $\beta_{vir} = 1$ .

The empirical relation between the virial parameter is  $\beta_{vir} = 2 a \beta$ , where  $\beta$  is the dimensionless ratio defined in Eq. 5 and  $a$  is a numerical factor that is empirically included to take modifications of non-homogeneous and non-spherical density distributions into account. According to this empirical relation, the virial parameter of the simulation of this paper is approximately 1.

Later, the virial theorem will be useful to show the level of virialization of the simulation outcome. In general terms, for a gas structure at virial equilibrium, the energy ratios defined above in Eqs.4 and 5 satisfy the relation

---

<sup>2</sup>We also consider models with a very high value of the ratio of the kinetic energy to the gravitational energy; in addition, there is observational interest in these kinds of model, see Section 2.2.1 below.



$$\alpha + \beta = \frac{1}{2}. \quad (7)$$

It is expected that if a gaseous system has  $\alpha + \beta > 1/2$ , then it will expand; in the other case, if  $\alpha + \beta < 1/2$ , then the system will collapse. It must be mentioned that Miyama et al. (1984), Hachisu and Heriguchi (1984) and Hachisu and Heriguchi (1985) obtained a criterion of the type  $\alpha \times \beta < 0.2$  to predict the output of a given simulation.

### 2.2.1. *Observational evidence for models with extreme initial kinetic energy.*

High kinetic energy molecular clouds have recently been observed. For example, Jackson et al. (2018), reported unusually large line-widths of the G337.342-0.119 gas structure, which is also known as the Pebble. These kinds of clouds are expected not to collapse in terms of the virial theorem, because a gas structure such as the Pebble reaches a virial parameter of 3.7.<sup>3</sup>

In spite of this, numerical simulations have shown that there are gas structures with a high kinetic energy, so that their virial parameter is around or greater than 2, and are in a state of global collapse, see for instance Ballesteros et al. (2018). In addition, Arreaga (2018) determined the extreme kinetic energy allowed for a turbulent core to collapse under the influence of its own self-gravity. The results that these authors found are given in terms of the ratio  $\beta$ , which is defined here in Eq. 5 of Section 2.2, so that a turbulent core can have an initial  $\beta$  as high as 2 – 8 and with an initial Mach number within 3 – 9 and still finish its evolution in a collapsed state.

For clouds in the CMZ, the gas is observed to be highly turbulent, with high non-thermal line-widths in the range from 20 to 50 km/s. Considering an isothermal sound speed within the range from 0.3 to 0.6 km/s for gas temperatures from 30 to 100 K, the typical Mach numbers are in the range from 10 to 60, which is a highly supersonic turbulence, see Bally et al. (1998) and Mills (2017).

### 2.3. *The azimuthal velocity*

Let us consider a massive agent, such as a dwarf spheroidal galaxy, which is located in the origin of a coordinate system. Let us place the molecular cloud of interest here to be in the

---

<sup>3</sup>Recall that the virial theorem states that a gas structure with a virial parameter less than 1 will collapse; otherwise, if the virial parameter is greater than 1, then a gas structure will not collapse.

z-axis, at a distance  $Z_C$ . This massive agent induces an escape velocity at each radius  $R$  (with respect to the center of the massive agent), so that

$$V_{\text{cir}} = \sqrt{2GM(R)/R} \quad (8)$$

where  $M(R)$  is the mass contained up to the radius  $R$  and  $G$  is Newton's gravitational constant. In spherical coordinates  $R, \theta$  and  $\phi$ , the velocity vector  $\vec{V}$  has components  $V_R, V_\theta$  and  $V_\phi$ , respectively. These spherical components are related to the Cartesian components of velocity  $V_x, V_y$  and  $V_z$  by three simultaneous equations, whose coefficients are given in terms of the sine and cosine of the polar and azimuthal angles  $\theta$  and  $\phi$ , as follows:

$$\begin{aligned} V_R &= V_x \sin(\theta) \cos(\phi) + V_y \sin(\theta) \sin(\phi) + V_z \cos(\theta) \\ V_\theta &= V_x \cos(\theta) \cos(\phi) + V_y \cos(\theta) \sin(\phi) - V_z \sin(\theta) \\ V_\phi &= -V_x \sin(\phi) + V_y \cos(\phi) \end{aligned} \quad (9)$$

Let us assume that  $Z_C$  and the radius of the cloud ( which is defined in Section 2  $R_0 = 3$  pc with respect to the center of the cloud), satisfy the relation  $R_0/Z_C \ll 1$ , then as  $\sin(\theta) = R_0/R \approx R_0/Z_C \ll 1$  then  $\theta \approx 0$ , for which  $\cos(\theta) \approx 1$  and  $\sin(\theta) \approx 0$ . In addition, in the particular case that the cloud follows a circular orbit around the massive center at radius  $R$ , then the velocity vector would only have a non-zero polar velocity component,  $V_\theta$ , while the radial and azimuthal components  $V_R$  and  $V_\phi$  are zero. Let us denote this velocity as  $V_\theta = -V_{\text{cir}}$ , where the minus sign indicates that the assumed rotation of the cloud is counter-clockwise in its orbit around the massive agent. Under these simplifications, the relations 9 between Cartesian and spherical components of velocity are reduced to

$$\begin{aligned} V_x &= -V_{\text{cir}} \cos(\phi) \\ V_y &= -V_{\text{cir}} \sin(\phi) \\ V_z &= 0 \end{aligned} \quad (10)$$

so that the magnitude of the velocity of a particle located at any radius  $R$  is therefore always given by  $\sqrt{V_x^2 + V_y^2} = V_{\text{cir}}$ . These Cartesian components of the velocity will be added to the particle velocity defined in Eq.1 to generate four new models in which this approximation will be implemented. It should be noted that the azimuthal angles have the same projection in both coordinate

systems: the first is based on the cloud center and the second is located at the gravitational agent center.

We will call this velocity the "azimuthal velocity" because it is given only in terms of the azimuthal angle  $\phi$ . Then, the approximation that replaces the tidal force by an azimuthal velocity, as described in Eq. 10, does not depend explicitly on the distance of the massive center to the cloud as long as ratio between the cloud radius to this distance is quite small.

Following with the model of a cloud of the CMZ, the mass of this massive agent has been fixed at  $M_B = 3.6 \times 10^6 M_\odot$ , which corresponds to the black hole located at the center of the Milky Way. In this case, the escape velocity at 500 pc is 5.57 km/s. To compare this velocity with those displayed at Fig.2, in terms of the speed of sound  $c_0$  defined in Section 2.2, we have a Mach number of  $V_{\text{cir}} = 2.47$ . It must be noted that the magnitude of this circular velocity  $V_{\text{cir}}$  is quite small as compared to that proposed by Molinari et al. (2011), in which a model for the orbit of the gas stream near the massive center Sgr B2 is around 80 km/s. For this reason, we have also included a second set of models in which the massive agent is considered to be molecular gas concentrated in the nuclear bulge of the Milky Way, see Launhardt et al. (2002), so that the total mass is  $M_H = 8.4 \times 10^8 M_\odot$ , see also Mills (2017), for which the escape velocity at 500 pc is 85 km/s, such that the normalized velocity in terms of the speed of sound 37.82.

#### 2.4. The collision models

It is important to emphasize that the cloud entirely contains the two subsets of particles that are going to collide. Let us call these subsets the pre-collision sub-clouds. They are located initially along the X-axis, so that the centers are: for the left-hand clump (-2.55,0,0) pc and for the right-hand clump (2.55,0,0) pc.

The radius of the pre-collision sub-clouds are chosen to be equal for two models, and different for other two models. The former models are head-on collisions. An impact parameter  $b$  has also been considered for the latter models, so that they are oblique collisions, in which the  $b$  takes the value 1.5 pc along the Y-axis. Bekki and Couch (204) have demonstrated observationally that the most likely impact parameter  $b$  in cloud collisions in the Large Magellanic Cloud and the Small Magellanic Cloud is  $0.5 D < b < D$  where  $D$  is the diameter of the cloud. For the radius  $R_0$  of the cloud considered in this paper,  $b$  has been chosen such that  $b = 0.25 D$ .

We show all these models in Table 1. The label is shown in column one. The impact parameter value is shown in column two. In columns three and four, the relationship of the radius

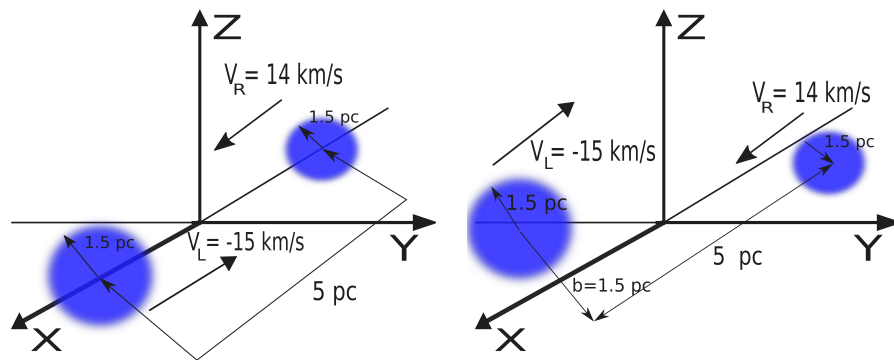


Fig. 1. Schematic diagram of the pre-collision geometry for (left-hand panel) a head-on collision and (right-hand panel) an oblique collision.

and translational velocities are shown, for the left-hand and right-hand sub-clouds, respectively. It is important to emphasize that the relative pre-collision velocity of the sub-clouds is 29 km/s and is formed for non-identical velocities for the left-hand and right-hand sub-clouds. In column five, the value of the ratio of the kinetic energy to the gravitational energy for the initial configuration of particles is shown, see Eq.5. Finally, column six gives the value of the azimuthal velocity added to the cloud particles, see Section 2.3. It must be clarified that these models are a sample from a larger set of models that was considered in a first manuscript, so that the numbers of the labels do not show any ordering.

#### 2.4.1. A note on the physical parameters chosen for the sub-clouds.

As we mentioned in Section 1, the idea that the Brick could be formed by a non-identical cloud-cloud collision has been explored for some time. Habe and Ohta (1992) assumed that the mass ratio of the colliding clouds is 1:4 and the radius ratio is 1:2. Later, Lis and Menten (1998) followed this collision model, so that their pre-collision velocities of the clouds are taken for this paper exactly as these author introduced them.

More recently, using observations, Kauffmann et al. (2013) estimated that the virial parameter of the Brick is around  $\beta_{\text{vir}} \leq 0.8$  and considered the same geometry of un-equal clouds at the same relation proposed by Habe and Ohta (1992) and Lis and Menten (1998). In this

TABLE 1

THE COLLISION MODELS;  $b$  IS THE IMPACT PARAMETER;  $r_L : r_R$  IS THE INITIAL RELATION OF THE COLLIDING SUB-CLOUD RADII;  $v_L : v_R$  IS THE RELATION OF THE TRANSLATIONAL VELOCITIES OR PRE-COLLISION VELOCITIES;  $\beta_0$  IS THE INITIAL RATIO OF KINETIC ENERGY TO GRAVITATIONAL ENERGY; AND  $V_{\text{CIR}}/c_0$  IS THE RATIO BETWEEN THE AZIMUTHAL VELOCITY AND THE SPEED OF SOUND .

model	$b$ [pc]	$r_L : r_R$ [pc]	$v_L : v_R$ [km/s]	$\beta_0$	$V_{\text{cir}}/c_0$
U5	0	0.75:1.5	14:-15	0.5	0
U13	0	1.5:1.5	14:-15	0.5	0
U9	1.5	0.75:1.5	14:-15	0.5	0
U11	1.5	1.5:1.5	14:-15	0.5	0
U5b	0	0.75:1.5	14:-15	50	0
U13b	0	1.5:1.5	14:-15	50	0
U9b	1.5	0.75:1.5	14:-15	50	0
U11b	1.5	1.5:1.5	14:-15	50	0
U5r	0	0.75:1.5	14:-15	0.5	2.47
U13r	0	1.5:1.5	14:-15	0.5	2.47
U9r	1.5	0.75:1.5	14:-15	0.5	2.47
U11r	1.5	1.5:1.5	14:-15	0.5	2.47
U5rb	0	0.75:1.5	14:-15	0.5	37.82
U13rb	0	1.5:1.5	14:-15	0.5	37.82
U9rb	1.5	0.75:1.5	14:-15	0.5	37.82
U11rb	1.5	1.5:1.5	14:-15	0.5	37.82

paper, we have taken the value of  $\beta_0 = 0.5$ , so that we expect to have a value of the virial parameter of  $\approx 1$ , see Section 2.2.

Shortly after, Higuchi et al. (2014) reconsidered this idea and continued the exploration of a cloud-cloud collision model in which the relative speed of colliding clouds was within the range from 30 to 60 km/s, and the radii were of 1.5 and 3 pc, for the small and big clouds, respectively.

In this paper, the translation velocity shown in Table 1,  $v_L : v_R$ , is given in terms of the sound speed  $c_0$  by 6.2:6.6 Mach, so that the relative velocity of approach is little greater than 12 Mach.

To allow comparison of the results of the present paper with these authors Lis and Menten (1998), Kauffmann et al. (2013) and Higuchi et al. (2014), we use here the values for the mass, radius and translation velocity of the cloud-cloud collision model that were used by these authors.

It must be noted that the gas particles of all the models described in Table 1 include the Cartesian components of velocity described in Eq.1, which are the turbulent velocity spectrum and the translation velocity  $v_L : v_R$  of the sub-clouds. However, only the last four models include a third set of velocity components already described Eq.10, which are needed to implement the approximation that replaces the tidal force by an azimuthal velocity. All of these three types of velocities enter as initial conditions of the SPH particles, as we will describe in Section 2.5.

### 2.5. Characterization of the initial turbulence

To show the nature of the turbulence that is implemented in Section 2.1.2, we consider the distribution functions of the initial velocity.

In Fig.2, we show the distribution functions of the radial component of the velocity at the initial snapshot, so that in the vertical axis the fraction  $f$  of the simulation particles whose magnitude of the velocity is smaller than that value shown in the horizontal axis. The radial component has been calculated with respect to the origin of the coordinates located in the center of the cloud, which is located at the center of the simulation box.

According to the left-hand column panels of Fig.2 that is, for models  $U$  and  $Ub$ , half of the simulation particles have negative radial velocity component, while the other half have a positive radial component. This symmetry is expected from the random process described in Section 2.1 to generate the direction of the velocity vectors.

It must be emphasized that for the right-hand column panels of Fig.2 that is, for models  $Ur$  and  $Urb$ , which include an azimuthal velocity, the symmetry of the curves with respect to the

positive and negative radial components has been lost. These panels indicate that the azimuthal velocity favor that 80 percent of the particles have negative radial component of the velocity.

It must also be emphasized that both types of models  $U$ ,  $Ur$  and  $Urb$  have the same initial turbulent velocity spectrum with the same level of energy, as defined in Section 2.1 and Section 2.2, and have the same translational velocity. The only difference between them is whether or not they include the azimuthal velocity, as described in Section 2.3. It is observed in Fig.2 that the distribution function of the models  $U$  shows a magnitude of the velocity 12 percent smaller than that of models  $Ur$ .

Later, we will compare these curves at the initial snapshot with curves obtained for an snapshot of the final evolution stage.

A brief description of the dynamics of the isolated cloud is given in Section 5.1.

### 2.6. The evolution code

The simulations of this paper are evolved using the particle-based Gadget2 code, which implements the SPH method to solve the Euler equations of hydrodynamics; see Springel (2005). Gadget2 has a Monaghan-Balsara form for the artificial viscosity, see Balsara (1995), so that the strength of the viscosity is regulated by setting the parameter  $\alpha_\nu = 0.75$  and  $\beta_\nu = \frac{1}{2} \times \alpha_\nu$ , see Equations 11 and 14 in Springel (2005). The Courant factor has been fixed at 0.1.

The SPH sums are evaluated using the spherically symmetric M4 kernel and so gravity is spline-softened with this same kernel. The smoothing length  $h$  establishes the compact support, so that only a finite number of neighbors to each particle contribute to the SPH sums. The smoothing length changes with time for each particle, so that the mass contained in the kernel volume is a constant for the estimated density. Particles also have gravity softening lengths  $\epsilon$ , which change step by step with the smoothing length  $h$ , so that the ratio  $\epsilon/h$  is of order unity. In Gadget2,  $\epsilon$  is set equal to the minimum smoothing length  $h_{\min}$ , which is calculated over all particles at the end of each time step.

### 2.7. Resolution

Truelove et al. (1997) demonstrated that the resolution requirement of a hydrodynamic simulation can be expressed in terms of the Jeans wavelength  $\lambda_J$ , which is given by

$$\lambda_J = \sqrt{\frac{\pi c^2}{G \rho}}, \quad (11)$$

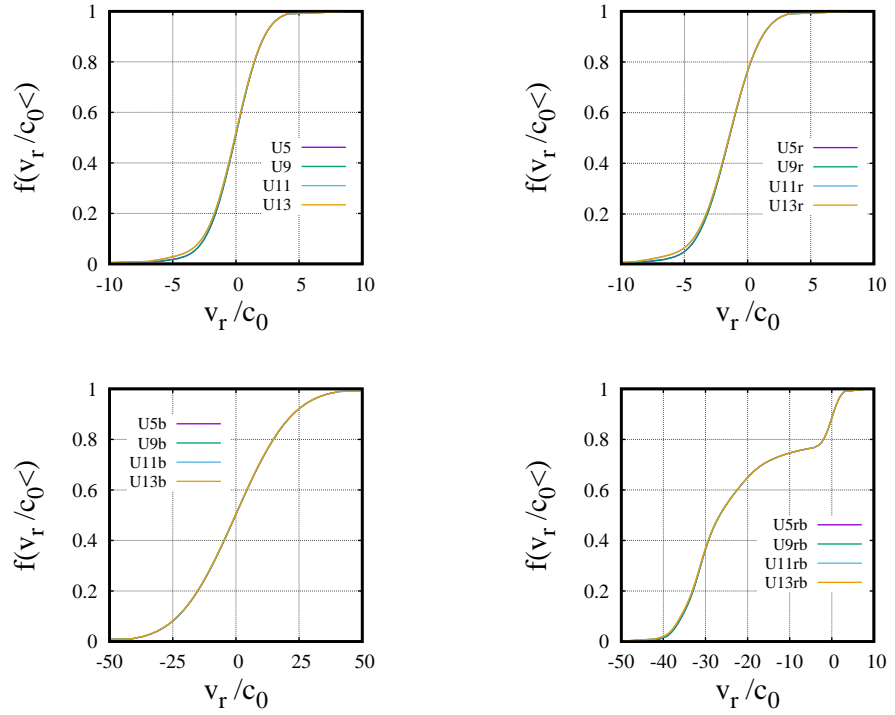


Fig. 2. Distribution function for the radial component of the velocity at the initial snapshot at  $t/t_{ff} = 0$ , for the model (top left-hand)  $U$  with a low level of turbulence; (top right-hand)  $Ur$  with a low azimuthal velocity; (bottom left-hand)  $Ub$  with a high level of turbulence and (bottom right-hand)  $Urb$  with a high azimuthal velocity.  $f$  is the fraction of particles whose magnitude of the velocity  $v_r/c_0$  (normalized with the sound speed) is smaller than that value shown in the horizontal axis.



where  $G$  is Newton's gravitation constant,  $c$  is the instantaneous sound speed and  $\rho$  is the local density, so that a mesh-based simulation must always have its grid length scale  $l$  such that  $l < \lambda_J/4$ .

Bate and Burkert (1997) demonstrated that the resolution requirement for a particle-based code, the Jeans wavelength  $\lambda_J$  is better written in terms of the spherical Jeans mass  $M_J$ , which is defined by

$$M_J \equiv \frac{4}{3}\pi \rho \left(\frac{\lambda_J}{2}\right)^3 = \frac{\pi^{\frac{5}{2}}}{6} \frac{c^3}{\sqrt{G^3 \rho}}. \quad (12)$$

so that an SPH code will produce correct results as long as the minimum resolvable mass  $m_r$  is always less than the Jeans mass  $M_J$ . The mass  $m_r$  is given by  $m_r \approx M_J/(2N_{neigh})$ , where  $N_{neigh}$  is the number of particles included in the SPH kernel (i.e., the number of neighbors). Therefore, our simulations will comply with this resolution requirement if the particle mass  $m_p$  is such that  $m_p/m_r < 1$ .

As we mentioned in Section 2.1, we have  $N = 13366240$  SPH particles in each simulation and therefore  $m_p = 7.4 \times 10^{-3} M_\odot$ . Now, if we consider that the highest peak density in our collision models is  $\rho_{\max} = 5.0 \times 10^{-12}$  g/cm<sup>3</sup>, then the minimum Jeans mass would be given by  $(M_J)_{\min} \approx 0.594048 M_\odot$ , so that, we obtain  $m_r = 7.4 \times 10^{-3} M_\odot$ . Thus, for that peak density the ratio  $m_p/m_r \leq 1$ , and the Jeans resolution requirement is satisfied. In this sense, we are sure to avoid the growth of numerical instabilities or the occurrence of artificial fragmentation in all our simulations up to densities smaller or equal than  $\rho_{\max}$ . In the next sections, we will present our results in terms of a normalized density, so that  $\log(\rho_{\max}/\rho_0)$  is given by 7.9, where  $\rho_0$  is the average density of the initial cloud, as we mentioned in Section 2.

### 2.8. Equation of state

Most simulations in the field of collapse used an ideal equation of state or a barotropic equation of state (BEOS), as was proposed by Boss et al. (2000):

$$p = c_0^2 \rho \left[ 1 + \left( \frac{\rho}{\rho_{\text{crit}}} \right)^{\gamma-1} \right], \quad (13)$$

where  $\gamma \equiv 5/3$  and  $\rho_{\text{crit}}$  is a critical density, a parameter which we explain now. This BEOS takes into account the increase in temperature of the gas as it begins to heat once that gravity has produced a substantial contraction of the cloud. In this paper, we also use this BEOS scheme for simplicity with a critical density  $\rho_{\text{crit}} = 5.0 \times 10^{-14}$  g/cm<sup>3</sup>, which is 100 times smaller than

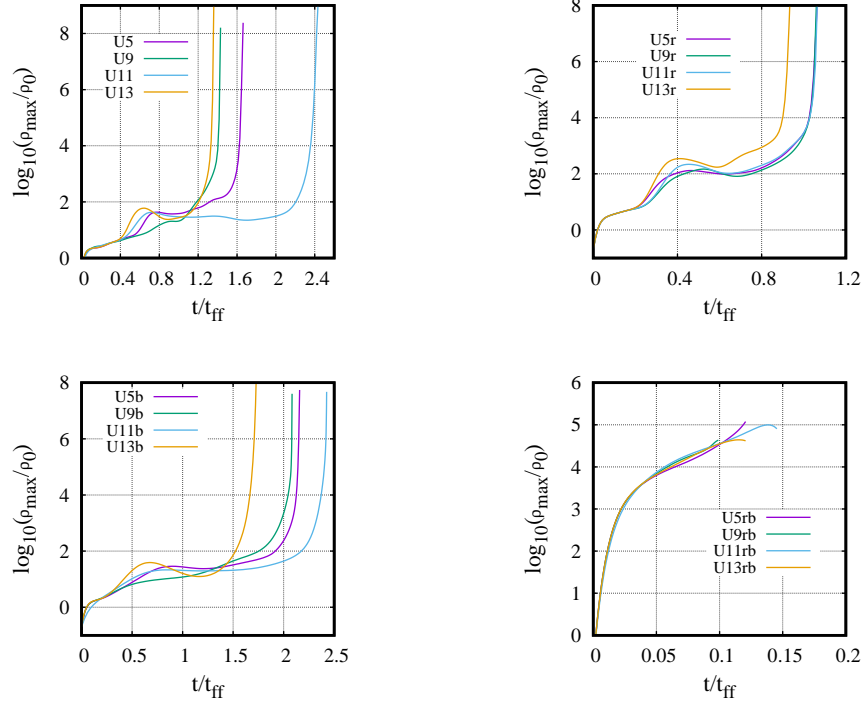


Fig. 3. Evolution of the density peak for all the models (top left-hand)  $U$  with low level of turbulence; (top right-hand)  $Ur$  with a low azimuthal velocity (bottom left-hand)  $Ub$  with high level of turbulence and (bottom right-hand)  $Urb$  with a high azimuthal velocity.

the peak density considered in Section 2.7 for the resolution requirement estimate; that is,  $\rho_{\max}$ . However, it should be emphasized that it is only an approximation. Consequently, to describe correctly the transition from the ideal to the adiabatic regime, one needs to solve the radiative transfer problem coupled to gravity in a self-consistent way.

### 3. RESULTS

#### 3.1. Evolution of the density peak

In Fig.3 we show the time evolution of the global density peak, irrespective of where the particle with the highest density is located in the simulation volume. As can be seen in this figure, all of the models collapse at different times (as expected).

Let us consider the top left-hand panel of Fig.3, the models with a low level of turbulence. The fastest collapse is that of model *U13*; followed by the collapse of models *U9* and *U5*, respectively. The slowest collapse is that of model *U11*.

This ordering seems to be a consequence of the gas dragging, which is caused by the asymmetry in radius and velocity. Consequently, as the gas flows, it is more difficult to condense by the action of the gravity. Model *U13* does not show any sign of gas dragging, because the gas remains of the head-on collision is still around of the pre-collision center. This is the reason why this model collapses first.

The density peak curve of the model *U9* very closely follows to that of model *U13*; This happens because the right-hand sub-cloud acts as a primary member in the binary system formed, which is only slightly perturbed by the left-hand sub-cloud, that acts as a secondary member of the binary. The collapse takes place first in the primary, which is more massive.

The density peak curve of the model *U5* is the third to reach the collapse. This happens because the right-hand sub-cloud entirely swallows the left-hand sub-cloud during the collision, so it produces a mass perturbation in the central region, which must first settle down for the collapse to continue. The slowest collapse is that of model *U11*. This happens because the dragging of the colliding sub-clouds is maximum, so the mass does not stack easily.

Let us now consider the bottom left-hand panel of Fig.3, the models *Ub* with a high level of turbulence. In this case, the behavior of all of the curves is the same as that explained earlier for the top panel, but for the panel of model *Ub* there is a slight shift to the right to longer evolution times, above all for the models *U5b*, *U9b* and *U13b*. The collapse time of model *U11b* is almost similar to that observed in model *U11*.

We observe a very significant change in the time scale for the right column panels of Fig.3; in the top right-hand panel, the models *Ur* that include a low azimuthal velocity, the collapse is accelerated, so that the collapse time is shorter than the previous models *U* and *Ub* by 40 percent, approximately. In the bottom right-hand panel, the models *Urb* that include a high azimuthal velocity, the collapse is extremely fast and the time scale has been reduced to a range from 0.1 to 0.15  $t/t_{ff}$ . In addition, the curves for the models *Urb* do not show any sign of the early random collisions between the SPH particles, due to the turbulence spectrum induced on each particle velocity.

### 3.2. Column density plots

The main outcome of the collision models is shown by means of column density plots of a thin slice of gas, parallel to the x-y plane. To make a proper comparison between the different models, we have selected for each model a snapshot whose peak density is such that  $\log(\rho_{\max}/\rho_0) \approx 5$ .

In model *U5*, once the head-on collision between the left-hand and right-hand sub-clouds has taken place, the asymmetry in the original sub-clouds in both radius and translational velocity, makes the right-hand sub-cloud (the biggest and the fastest cloud) swallow and drag the left-hand sub-cloud (the smallest and slowest cloud). The resulting stirred gas oscillates from the left-hand side to the right-hand side along the x-axis. The spatial symmetry in the original configuration of the right-hand sub-cloud is translated to the symmetry in the arms developed around the central cloudlet, as can be seen in the top left-hand panel of Fig.4. In Section 3.1, this phenomenon was simply referred to as gas dragging, which was a useful way to explain the time of collapse by means of the density peak curves.

When the asymmetry in the radius is removed, the final result is a central cloudlet, that is elongated along the x-axis, with a strong bipolar outflow along the y-axis, as can be seen in the top right-hand panel of Fig.4, which is the outcome of model *U13*. Because of this result, we note that the asymmetry in the velocities of the collision model is not as important as the asymmetry in the radii with respect to the outcome of the simulations.

Different results are obtained when an impact parameter is taken into account. In the case of model *U9*, as illustrated in the bottom left-hand panel of Fig.4, the asymmetry in the radii and velocities together with an impact parameter produce a weak binary system, in which the left-hand sub-cloud (the smallest and slowest cloud) passes by and is attracted by the right-hand sub-cloud (the biggest and fastest cloud), so that part of the mass of the former is pulled out. Nevertheless, an arm is still visible around the remains of the pre-collision left-hand sub-cloud and a long arm is also developed around the central cloudlet, which is analogous in origin to the arm formed in model *U5*.

In the case of the model *U11*, when the symmetry in the radii of the pre-collision sub-clouds is restored but still in the presence of the impact parameter as in model *U9*, a binary system is formed as the main outcome, in which several gas bridges are seen to be strongly connecting strongly the remains of the two colliding clumps, as can be seen in the bottom right-hand panel

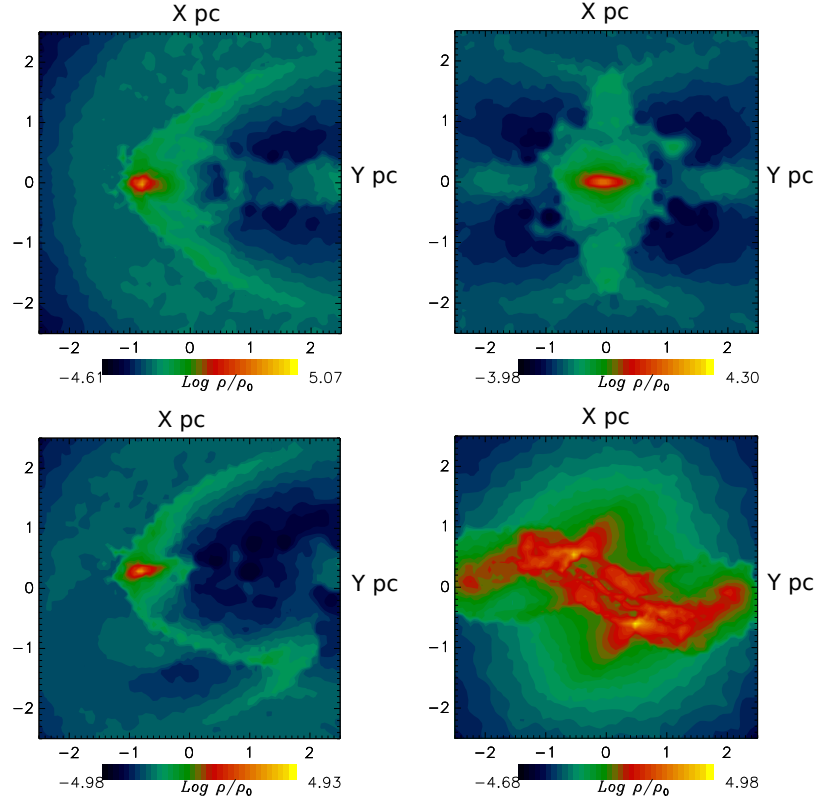


Fig. 4. Column density plots of the collision models  $U$ , for a thin slice of gas parallel to the x-y plane. The unit of length is one parsec. The models are shown in panels as follows: (top left-hand)  $U5$  (at time  $t/t_{ff} = 1.65$  and peak density  $\log(\rho_{\max}/\rho_0) = 5.0$ ); (top right-hand)  $U13$  (at time  $t/t_{ff} = 1.34$  and peak density  $\log(\rho_{\max}/\rho_0) = 4.3$ ); (bottom left-hand)  $U9$  (at time  $t/t_{ff} = 1.42$  and peak density  $\log(\rho_{\max}/\rho_0) = 5.0$ ); (bottom right-hand)  $U11$  (at time  $t/t_{ff} = 2.4$  and peak density  $\log(\rho_{\max}/\rho_0) = 5.0$ ).

of Fig.4.

In Fig.5 we show the column density plots of the models  $Ub$ , with a high level of turbulence. As expected, there is a lot of similarity with the previous models  $U$ , with a low level of turbulence, because the initial structure of the velocity spectrum is the same for both models  $U$  and  $Ub$ . The only difference is the magnitude of the velocity. The larger magnitude of the velocity for models  $Urb$  makes the arms and tails larger and better defined than those in models  $U$ .

Let us now consider the iso-density plots for models  $Ur$ , which are shown in the Fig.6. In this case, we show two columns of density plots. In the right-hand column of Fig.6, we show the density plots for the snapshots with almost the same density peak shown in Fig.4 to allow comparison with models  $U$  and  $Ub$ . We only observe an homogeneous and spherical collapse as the final result of simulations  $Ur$ .

In the left-hand column of Fig.6, we choose snapshots of the first stage of evolution, to show the early development of a central lump of gas, which is a direct consequence of the azimuthal velocity added to the particle velocity, see Section2.3. This central lump of gas makes the collapse of the cloud faster, as can be seen in Fig.3, because it acts as a centrally located mass attractor.

Finally, let us consider the iso-density plots for models  $Urb$ , which are shown in Fig.7. We observe the formation of a massive lump of gas at the cloud center, at the beginning of the evolution, similarly to those shown in the left-hand column of Fig.6. However, for each model  $Urb$ , the massive lump of gas is quite more bigger than for models  $Ur$ . This is a direct consequence of the higher azimuthal velocity added to the particle velocity, see Section2.3. This massive central lump of gas makes the collapse quite faster than that observed for models  $Ur$ , as we notice happens in the bottom right-hand panel of Fig.3.

### 3.3. 3D rendered plots

In Fig.8, we show the spatial structure of the models  $U$  using 3D plots, for the same time and density chosen for the snapshot shown in Fig.4. Until now, the figures displayed in Section 3.2, have been cuts parallel to the equatorial plane of the initial sphere, so that around of 10,000 particles are included in the slice shown. For the 3D plots, all of the particles with a density greater than  $\log(\rho_{\max}/\rho_0) \approx 0.7$  and located within the region  $[-2.5, 2.5]$  in the three Cartesian coordinates  $x, y, z$ , entered in the 3D plots. In this case, the number of particles that are used to make the 3D plots ranges from 181266 to 5616884. The log of the density is rendered in the 3D plots to assign a color and a vertical bar located in the bottom right-hand corner of each panel. It must be noted

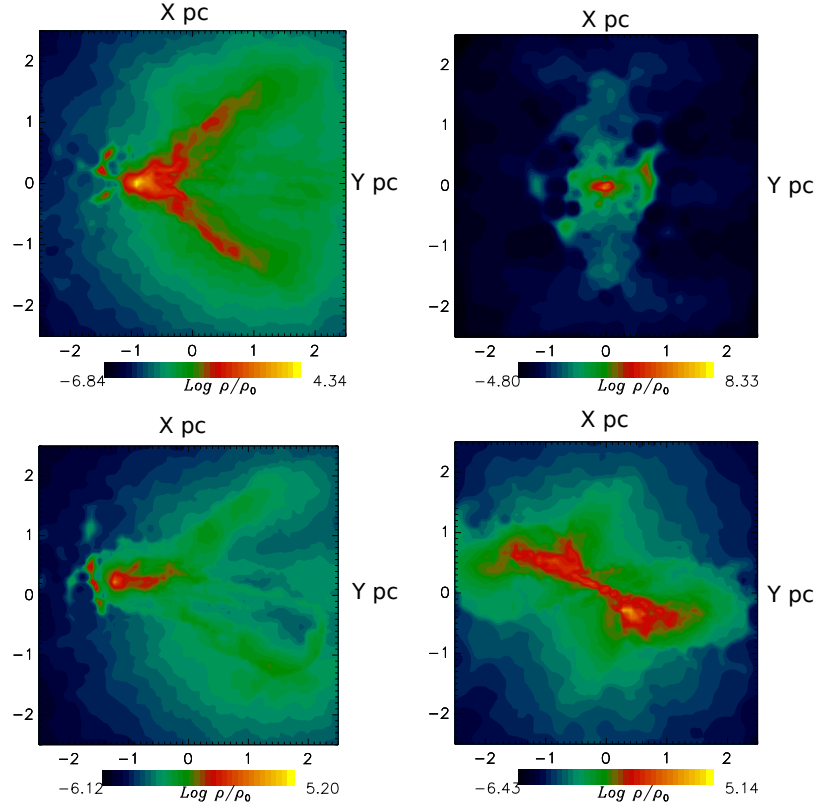


Fig. 5. Column density plots of the collision models  $Ub$ , for a thin slice of gas parallel to the x-y plane. The unit of length is one parsec. The models are shown in panels as follows: (top left-hand)  $U5b$  (at time  $t/t_{ff} = 2.15$  and peak density  $\log(\rho_{\max}/\rho_0) = 4.34$ ); (top right-hand)  $U13b$  (at time  $t/t_{ff} = 1.73$  and peak density  $\log(\rho_{\max}/\rho_0) = 8.63$ ); (bottom left-hand)  $U9b$  (at time  $t/t_{ff} = 2.08$  and peak density  $\log(\rho_{\max}/\rho_0) = 5.20$ ); (bottom right-hand)  $U11b$  (at time  $t/t_{ff} = 2.42$  and peak density  $\log(\rho_{\max}/\rho_0) = 5.14$ ).

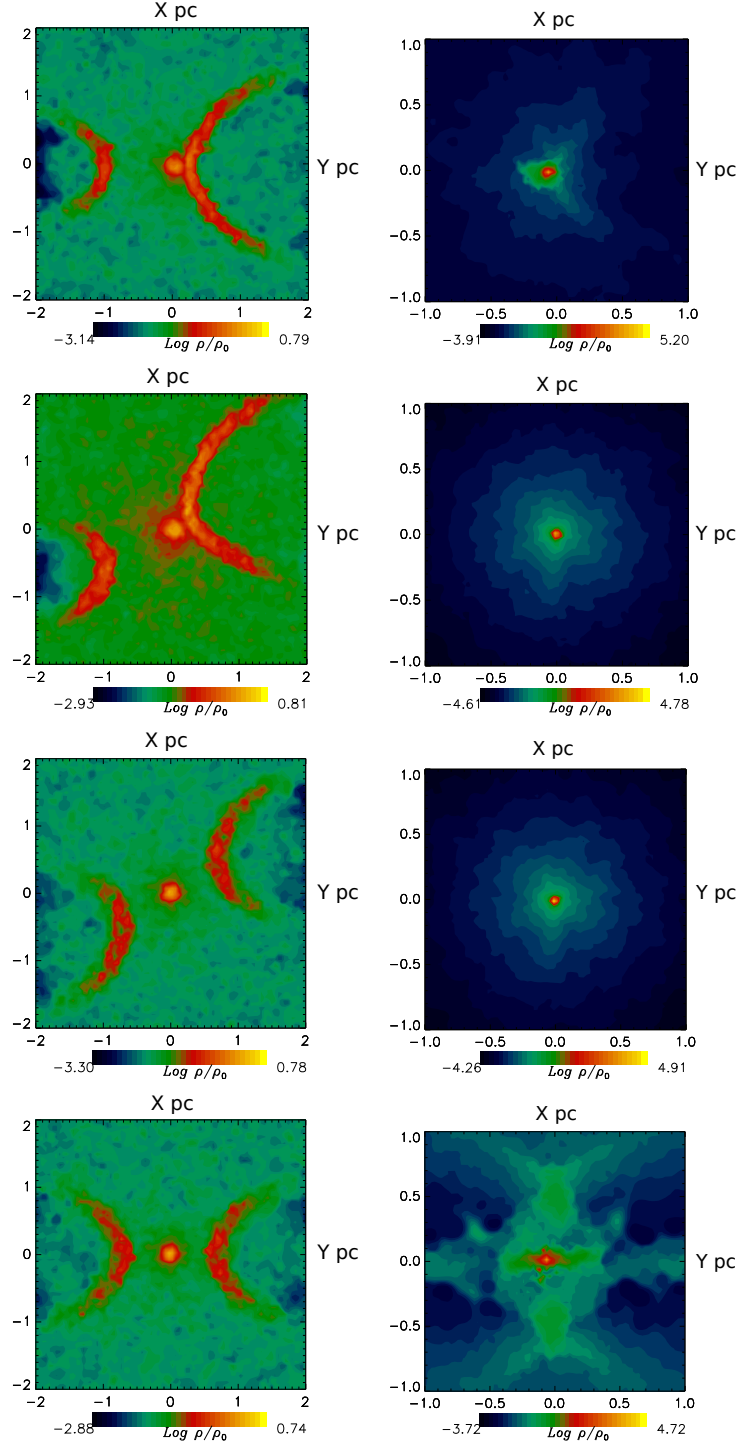


Fig. 6. Column density plots of the collision models  $U_r$ , with an azimuthal velocity included, see Section 2.3. The models are shown in panels (from top to bottom) as follows: (first line) Model  $U_{5r}$ , (left) at time  $t/t_{ff} = 0.24$ , peak density  $\text{Log } (\rho_{\max}/\rho_0) = 0.79$  and (right) at time  $t/t_{ff} = 1.05$ , peak density  $\text{Log } (\rho_{\max}/\rho_0) = 5.2$ ; (second top line) Model  $U_{9r}$ , (left) at time  $t/t_{ff} = 0.25$ , peak density  $\text{Log } (\rho_{\max}/\rho_0) = 0.8$  and (right) at time  $t/t_{ff} = 1.05$ , peak density  $\text{Log } (\rho_{\max}/\rho_0) = 4.8$ ; (third line) Model  $U_{11r}$ , (left) at time  $t/t_{ff} = 0.23$ , peak density  $\text{Log } (\rho_{\max}/\rho_0) = 0.78$  and (right) at time  $t/t_{ff} = 1.05$ , peak density  $\text{Log } (\rho_{\max}/\rho_0) = 4.9$ ; (fourth line) Model  $U_{13r}$ , (left) at time  $t/t_{ff} = 0.22$ , peak density  $\text{Log } (\rho_{\max}/\rho_0) = 0.74$  and (right) at time  $t/t_{ff} = 0.92$ , peak density  $\text{Log } (\rho_{\max}/\rho_0) = 4.7$ .



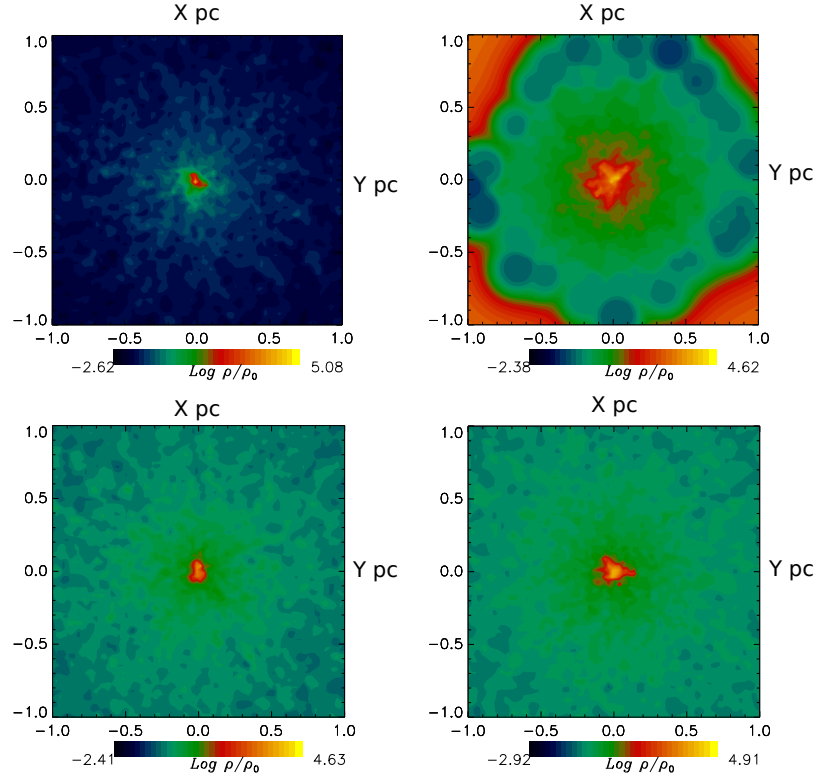


Fig. 7. Column density plots of the collision models  $Urb$ , for a thin slice of gas parallel to the x-y plane. The unit of length is one parsec. The models are shown in panels as follows: (top left-hand)  $U5rb$  (at time  $t/t_{ff} = 0.12$  and peak density  $\log(\rho_{\max}/\rho_0) = 5.0$ ); (top right-hand)  $U13rb$  (at time  $t/t_{ff} = 0.12$  and peak density  $\log(\rho_{\max}/\rho_0) = 4.62$ ); (bottom left-hand)  $U9rb$  (at time  $t/t_{ff} = 0.09$  and peak density  $\log(\rho_{\max}/\rho_0) = 4.63$ ); (bottom right-hand)  $U11rb$  (at time  $t/t_{ff} = 0.15$  and peak density  $\log(\rho_{\max}/\rho_0) = 4.62$ ).

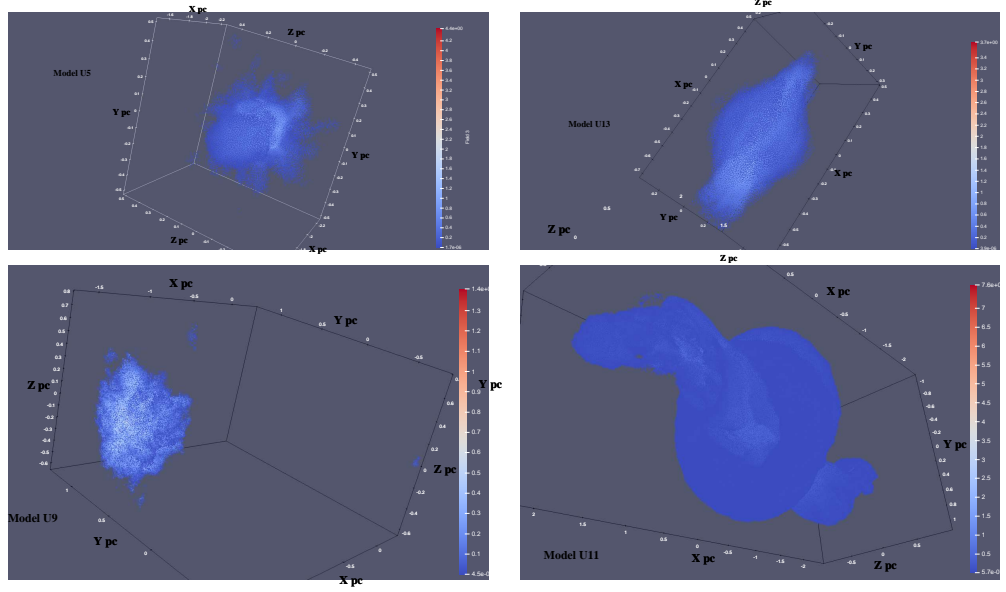


Fig. 8. 3D-plots of the collision models  $U$  for the same snapshots of Fig.4, rotated arbitrarily to reveal more details of the configurations, in a window of spatial dimension from -2.5 to 2.5, in each of the axis-XYZ, in which only those particles with  $\log(\rho_{\max}/\rho_0) > 0.7$  have entered to make the plot. The panels and the number of particles entered are shown as follows: (top left-hand)  $U5$  with 243455 particles; (top right-hand)  $U13$  with 287037 particles; (bottom left-hand)  $U9$  with 181266 particles and (bottom right-hand)  $U11$  with 5616884 particles.

that an arbitrary rotation is done on the Cartesian coordinates to show some of the details of the spatial structure.

In the top left-hand panel of Fig.8, we see the remains of the model  $U5$ , view from the rear (along the positive X-axis), in which one can see an elongated bulb. In the region where the un-equal sub-cloud collision takes place, on the negative side of the X-axis, one can see a thick disk of gas surrounding the elongated bulb. This structure looks like a mushroom pointing toward the negative X-axis.

In the top right-hand panel of Fig.8, we see the remains of model  $U13$ ; recall that this collision is head-on along the X-axis between two equal sized sub-clouds. For this reason, one can see an elongated solid tube of gas along the X-axis, surrounded by an almost spherical gas region, which is formed by the particles bounced from the collision, most of which escape away along the Y-axis in both directions, positive and negative.

In the bottom left-hand panel of Fig.8, we see the remains of model  $U9$ , in which two un-equal sized sub-clouds have an oblique collision. One can see only the remains of each separate sub-clouds, after their close encounter, so one can notice that the bottom sub-cloud is almost destroyed by the tidal force caused by the top sub-cloud.

In the bottom right-hand panel of Fig.8, we see the remains of model  $U11$ , in which two equal-sized sub-clouds have an oblique collision. For this reason, the symmetry is evident between the top and bottom gas tubes, which are formed as the tracks of the original colliding sub-clouds. There is a complex bridge of gas connecting these top and bottom tubes. A disk of gas is surrounding the bridge.

### 3.4. Distribution function of the radial component of velocity

In Fig.9 we show in the vertical axis the fraction of particles with a velocity smaller than that shown in the horizontal axis. This distribution function of the velocity is taken at the same time and density as the snapshots shown in Figs.4, 5, 6 and 7. We consider only the radial component of the velocity, which is calculated with respect to the center of the cloud.

By comparing with the panels of Fig.2 in Section 2.5, one can see that the fraction of the simulation particles with a negative component of the radial velocity has increased from 0.5 at time  $t/t_{ff} = 0$  for all the models, to 0.9 for models  $U$ , at time of the Fig.4; to 0.8 for models  $Ub$  and to 0.9 for models  $Ur$ . This means that a high fraction of the simulation particles have likely reached already (models  $U5$ ,  $U9$  and  $U13$ ) or are flowing towards (model  $U11$ ) an accretion center.

## 4. DYNAMIC CHARACTERIZATION OF THE SIMULATIONS OUTCOME

Let us define a cloudlet as the densest region of a simulation outcome, whose physical properties must be determined. The center of the cloudlet and a radius are the main parameters to delimit the cloudlet region and calculate its physical properties. These centers do not coincide in general the center of mass of each simulation, although both kind of centers are close to each other, as can be seen in Fig.10, in which we show the center of each cloudlet in models  $U$ .

### 4.1. Radial profile of the density and mass

In Fig.11 we show the radial profile of the density (in the left-hand column) and the mass (in the right-hand column), calculated with respect to the center of each cloudlet as defined in Fig.10.

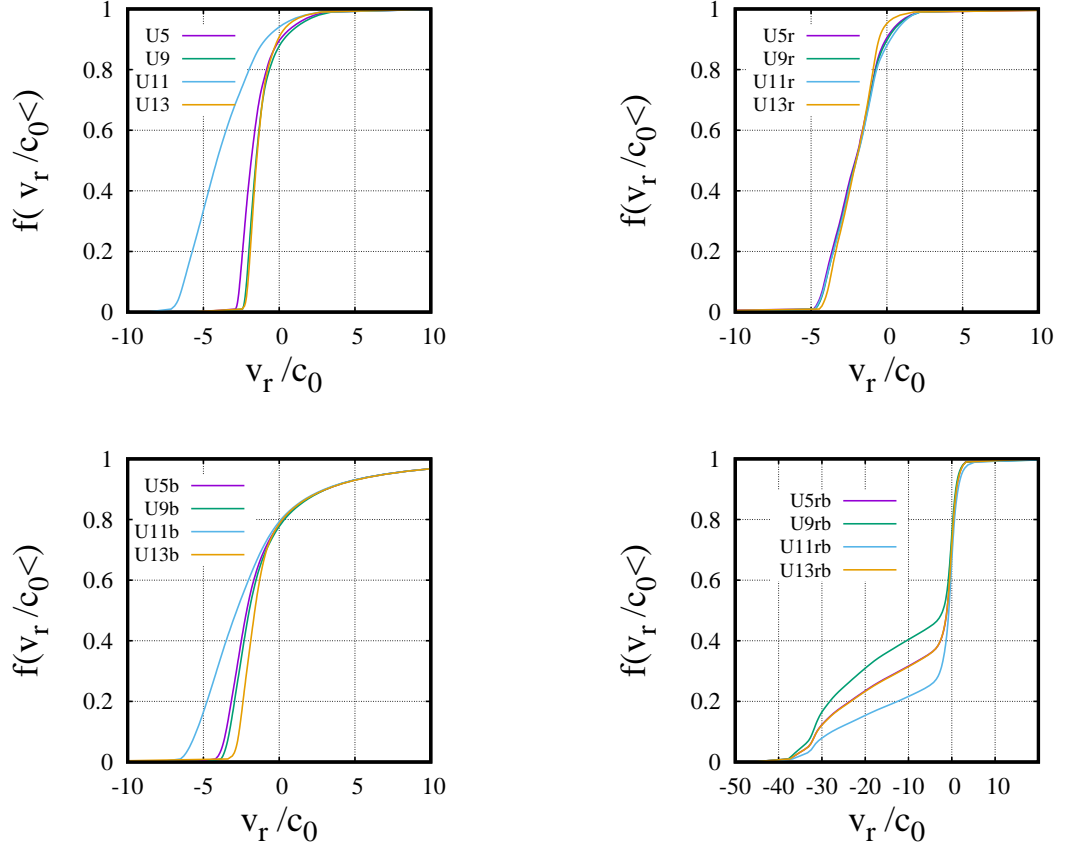


Fig. 9. Distribution function of the the radial component of the velocity, calculated with respect to the center of the cloud. The snapshot are taken at the same time and density of the snapshots shown in Fig.4, 5, 6 and Fig.7. (top left-hand) models  $U$  with a low level of turbulence; (top right)-hand  $U_r$  with a low azimuthal velocity (bottom left-hand)  $U_b$  with high level of turbulence and (bottom right-hand)  $U_{rb}$  with a high azimuthal velocity.

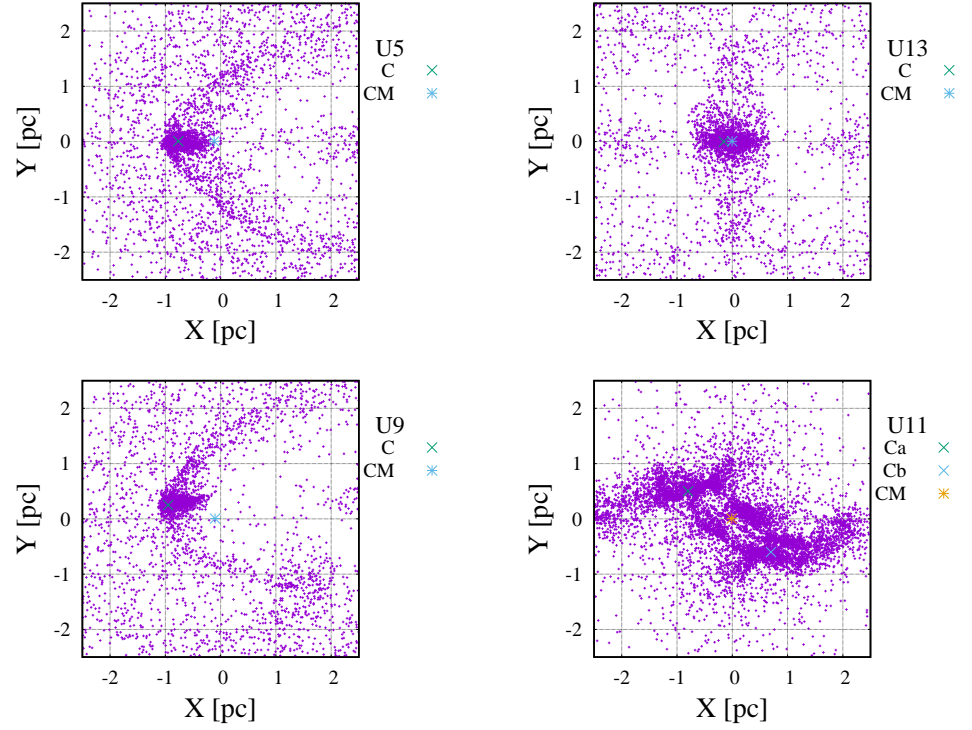


Fig. 10. Cloud centers are marked with a symbol "x"; the center of mass is marked with the symbol "\*"; both of them are located in a thin slice parallel to the XY plane, in which the symbol "+" represents a gas particle. The models are as follows: (top left-hand) *U5*; (top right-hand) *U13*; (bottom left-hand) *U9* and (bottom right-hand) *U11*.

It must be clarified that the density  $\rho_{\text{bin}}(r)$  and mass  $M(r)_{\text{bin}}$ , shown in the vertical axis of Fig.11, are determined by taking into account only those particles located within the radii  $r$  and  $\delta r$ , where  $\delta r$  is given by 4/500 pc per bin, and the  $r$  goes from  $r = 0$  (the cloudlet center) to  $r_{\text{max}} = 4$  pc (even further than the edge of the cloudlet, because we want to study the environment of the cloudlets as well).

Let us consider the top line of Fig.11 for models  $U$ . For model  $U11$ , there are two cloudlets. Consequently, we label the cloudlet located to the left of the vertical axis and above the horizontal axis, as cloudlet "a" (in the upper left-hand region). We label the cloudlet located to the right of the y-axis and below the x-axis as cloudlet "b", as can be seen in the bottom right-hand panel of Fig.10.

The curves of  $\rho_{\text{bin}}$  for the models  $U5$ ,  $U9$ ,  $U11a$  and  $U11b$  are not steep, as opposed to the curve for model  $U13$ . This means that the cloudlets of these models must have a mass increasing with radius, as can be seen in the right-hand panel of the top line of Fig.11.

Model  $U13$  is the only one that shows a density curve  $\rho_{\text{bin}}(r)$  decreasing significantly with radius  $r$ . For this behavior, the mass  $M(r)_{\text{bin}}(r)$  is almost kept constant for an wide range of radii. This would be the standard behavior of a dense cloudlet formed by gravitational attraction in a simulation.

In the second and third lines of Fig.11, from top to bottom, we show the curves for models  $Ub$  and  $Ur$ , respectively. The behavior observed here is quite similar to the one described earlier for model  $U$ . In the bottom line, we show the curves for models  $Urb$ , which include a high azimuthal velocity and we have seen in Section 3.2, the simulation outcome changed significantly. In this case, the density curves are kept constant and the mass curves are slightly increasing functions of the radius, above all in the range of radius 0-3 pc.

Rathborne et al. (2015) found curves for the radial profile of the mass and density of the Brick, such that the mass curve is always an increasing function of their effective radius, while the density curve is always a decreasing function, both curves extended up to a effective radius of 2 pc. For instance, the mass contained within its central one pc is approximately  $6 \cdot 10^3 M_{\odot}$ , while the density curve follows a power-law over radii  $r^{-1.2}$ .

The increasing mass curves shown in the right-hand column of Fig.11 are of the same order of magnitude as those reported by Rathborne et al. (2015), taking into account that the curves of Fig.11 are not cumulative (as we mentioned earlier). Therefore, the exterior layers (outside of the densest central region) of the cloud, contain a substantial amount of mass.

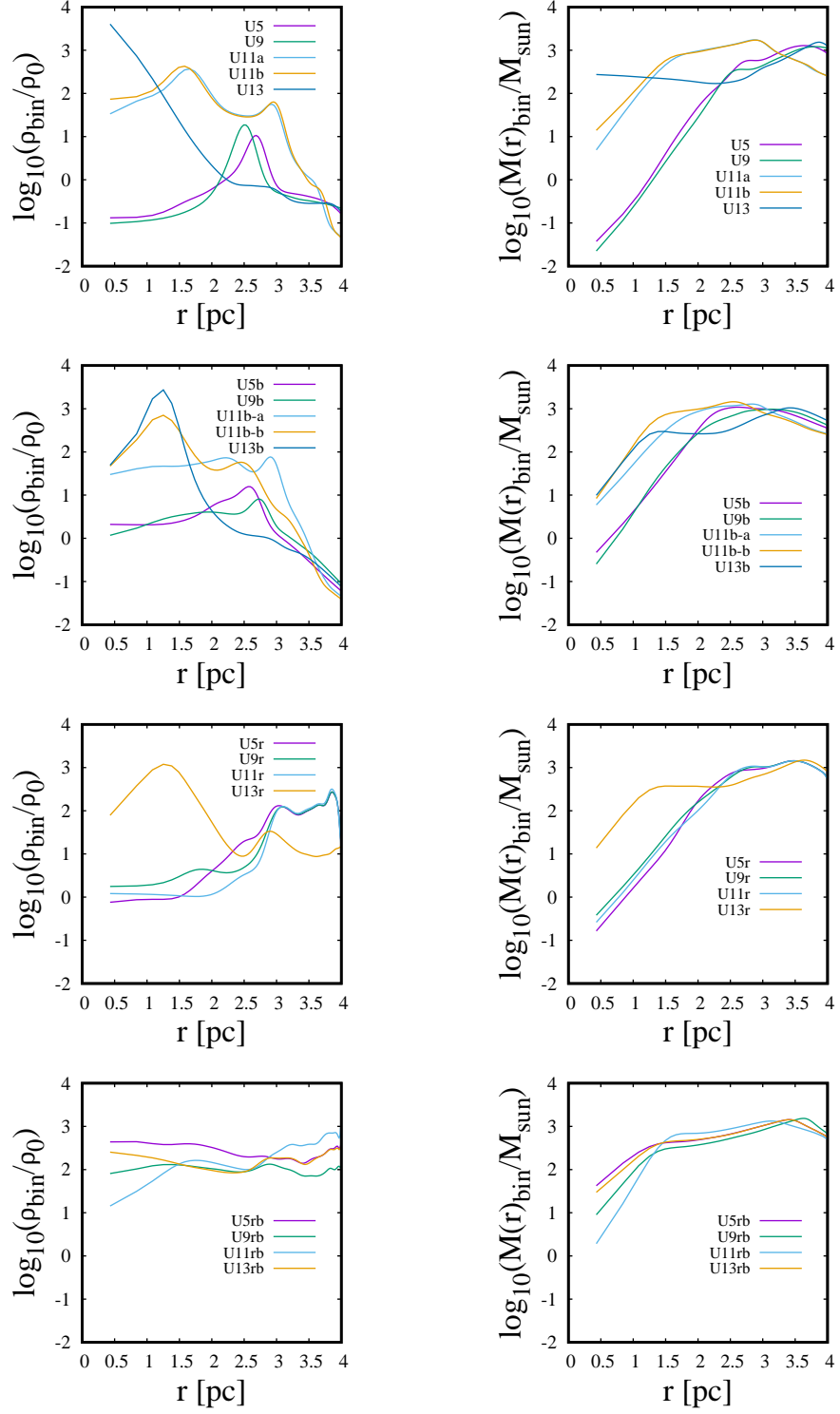


Fig. 11. (left-hand panel) Radial profile of the density and (right-hand panel) radial profile of the mass. In the vertical axis we show the mass and density averaged over those particles located within the radial spherical shell defined by  $r$ , so that these functions are not cumulative. In the horizontal axis,  $r$  starts at 0, the center of each cloudlet, as illustrated in Fig.10 for models  $U$  and analogously calculated for all the other models. The panels on the top line are for models  $U$ ; the panels on the middle line are for models  $Ur$  and the panels on the bottom line are for models  $Urb$ . The snapshots are taken at the same time and peak density shown in Fig.4, Fig. 5, Fig.6 and Fig.7, respectively.

#### 4.2. Radial profile of the radial and tangential components of the velocity

In Fig.12, we show the radial profile of the radial (left-hand column) and tangential (right-hand column) components of the velocity. We apply here the same radial partition described in Section 4.1; that is, from the cloudlet center up to 4 pc.

Let us clarify the meaning of the tangential component of the velocity. In spherical coordinates  $(r, \theta, \phi)$ , a gas particle has a magnitude of the velocity vector  $v_p$  with the components  $v_r, v_\theta$  and  $v_\phi$ . Then, we split the components of the velocity in radial  $v_r$  and tangential  $v_t = (v_\theta + v_\phi)/2$ , so that we can follow both components separately. We do this separation because the radial component can be associated with a collapse trend while the tangential component can be considered as a manifestation of turbulence, see Guerrero and Vázquez (2020).

The left-hand column panels Fig.12 indicates that many particles move to the cloudlet center, mostly from the innermost region of the cloud. The right-hand column panels Fig.12 indicate that there is a non-zero, almost constant, tangential component of the velocity. These observations indicate that a lot of particles are falling towards the cloudlet center in trajectories that are slightly curved (i.e., not from a purely radial direction, such as in a free-fall).

Let us recall the behavior of a test particle and let its velocity magnitude be given by  $v_g$ . This  $v_g$  is determined by  $v_g = \sqrt{2GM(r)/r}$ , where  $M(r)$  is the mass contained up to radius  $r$  and  $G$  is the Newton's gravitational constant. This  $v_g$  can be considered as the velocity when a test particle arrives at distance  $r$  from the central mass  $M$ , having started from rest at infinity, where its gravitational potential is zero. As is well-known, for a spatially bounded mass of radius  $R_g$ , the velocity  $v_g$  must increase with the radius  $r$ , such that  $0 < r < R_g$ . Once the radial coordinate  $r$  is outside the bounded mass- that is, for  $r > R_g$  the velocity  $v_g$  simply decreases.

It must be noted that a significant fraction of the total velocity magnitude  $v_p$  comes from its radial component  $v_r$ , though a minor fraction of  $v_p$  comes from the tangential components grouped in  $v_t$ . Then, we can think about a curve of  $v_p$  if we see a curve of  $v_r$ , because we only need to transform from  $v_r$  to  $v_p$  by changing the velocity sign, from negative to positive values, so that the behavior of both curves  $-v_r$  and  $v_p$  would have a lot of similarity.

Let us consider the panels of the top line of Fig.12, which are for models  $U$ . In terms of the "imagined curves" of  $v_p(r)$ , the cloudlets  $U11a$  and  $U11b$  follow the behavior expected for the test particle velocity, indicating that the cloudlet radius  $R$  (the analog of the bonded mass) is around 1 pc for both cloudlets of model  $U11$ . The curves for models  $U9$  and  $U13$  indicate that the



bounded mass has a very small radius  $R$ , which is slightly smaller than 0.5 pc. For model  $U5$ , the resolution of the radial partition is not fine enough to indicate a radius  $R$  of the cloudlet found. This bounded mass can be identified with the size of the region from the center of the cloud, which is a particle reservoir, out of which the particles flow towards the cloud center. The core of the collapsing cloud, which is formed by the particles with higher density of the simulation, is located in these cloud centers.

The panels of the second line of Fig.12, from top to bottom, show the curves for the models  $Ub$ , which are very similar to those already described for models  $U$ .

The panels of the third line of Fig.12, which are for models  $Ur$ , with a low azimuthal velocity, indicate a behavior very similar to that observed for models  $U9$  and  $U13$ , that is, a region of particle reservoir is about 1 pc in radius from the center of the cloud. These behaviors can be better seen in the panels on the bottom line of Fig.12, which are for models  $Urb$ . These models  $Urb$  have a high azimuthal velocity, whose effect is more clearly seen because the in-fall velocity is quite higher than in the previous models  $U$ ,  $Ub$  and  $Ur$ . Instead of a bounded mass, the size of the region of strong in-fall gas is determined by the size of the centrally located lump of gas induced by the azimuthal velocity, see the left-hand column of Fig.6, for an illustration.

### 4.3. Integral properties of the cloudlets

In Fig.13 we show the values of the dimensionless ratios  $\alpha$  and  $\beta$ , respectively, calculated only for a cloud region that includes the cloudlets and their surroundings. Two parameters are used: the first parameter is  $\log(\rho_{\min})$ , which is a lower bound for density; and the second parameter  $r_{\max}$  is a maximum radius, which is taken with respect to the cloudlet's center. To calculate the ratios  $\alpha_f$  and  $\beta_f$  for the cloudlets, we consider only those particles that have a density greater than  $\log(\rho_{\min})$  and are located at a radius smaller than  $r_{\max}$ . To make a comparison between all the models, to calculate the properties of all the models shown in Fig.13, we have used the following values  $\log(\rho_{\min}) = 0.0$  and  $r_{\max} = 1.5$  pc.

One can see in the top left-hand panel of Fig.13 that the models  $U5, U9$  and  $U13$  have a similar value for the ratio  $\alpha_f$ , which is around 0.1. For the cloudlets "a" and "b" of model  $U11$  (i.e.,  $U11a$  and  $U11b$ )  $\alpha_f$  is around 0.05. The values of the ratio  $\beta_f$  ranges from 0.1 for model  $U13$ , around 0.13 for model  $U5$ , and a little higher than 0.2 for model  $U9$ . Cloudlets  $U11a$  and  $U11b$  have the highest values of  $\beta_f \approx 0.55$ . Cloudlets  $U11a$  and  $U11b$  are the only ones over-virialized, because their sum  $\alpha_f + \beta_f > 1/2$ ; while the models  $U5, U9$  and  $U13$  are sub-virialized, because

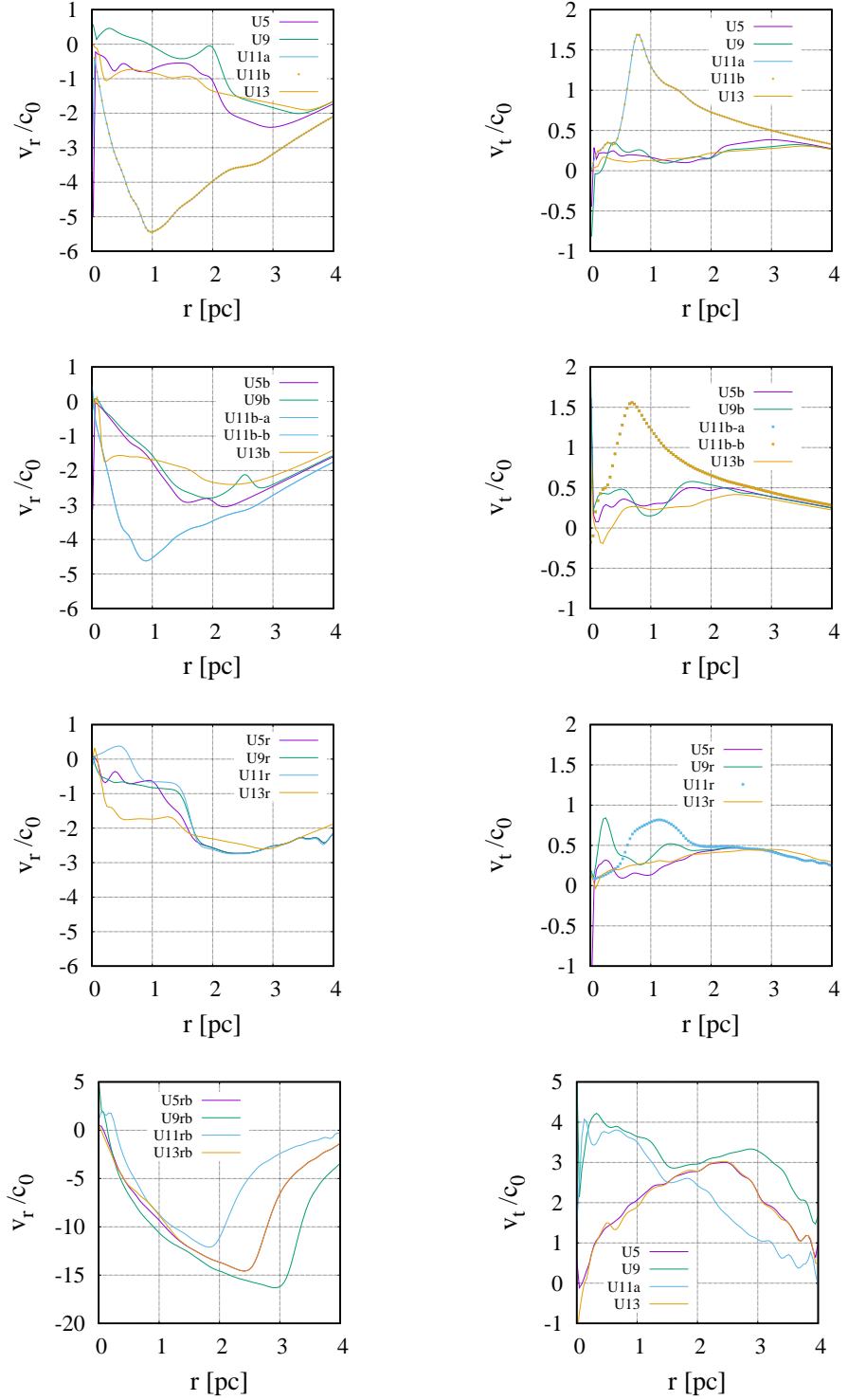


Fig. 12. (left-hand column) Radial profile of the radial component of the particle velocity and (right-hand column) the radial profile of the tangential component of the particle velocity, both calculated with respect the center of each cloudlet illustrated in Fig.10 and normalized with the speed of sound. From top to bottom, the first line of panels is for the models  $U$ ; the second line is for models  $Ub$  and the third and four lines are for models  $Ur$  and  $Urb$ , respectively. The snapshot considered for these calculations are those at the same time and peak density shown in Fig.4, Fig. 5, Fig.6 and Fig.7, respectively.

their sum  $\alpha_f + \beta_f < 1/2$ . The same behavior is observed for models *Ub*, with a high turbulence, as can be seen in the bottom left-hand panel of Fig.13.

In both the top right-hand panel and the bottom left-hand panel of Fig.13, we see that curves for the models *Ur* and *Ub*, respectively, show a behavior that is very similar to that already observed for the curves of models *U*. For all models *Ur* and *Ub* the ratio  $\alpha_f$  is around the value 0.09, with a clear tendency to lower values. The ratio  $\beta_f$  for these models ranges from 0.1 to 0.5. Models *Ur*, *Ur5*, *Ur9* and *Ur13* are sub-virialized, because their sum  $\alpha_f + \beta_f < 1/2$ . Meanwhile, for the two cloudlets of model *Ur11* are over-virialized, because their sum  $\alpha_f + \beta_f > 1/2$ . The same behavior is observed for models *Ub*.

On the opposite side, all models *Urb*, as shown in bottom right-hand panel of Fig.13, are over-virialized, because the high initial azimuthal velocity is manifested in the excess of kinetic energy, such that the  $\beta_f$  ratio for these models is in the range 7-11. In spite of this excess of kinetic energy, all models *Urb* have collapsed.

We show the mass associated with the cloudlets of the models on the vertical axis of Fig.14. We have considered the mass of only those particles that entered into the calculation of the physical properties shown in Section 4. In the horizontal axis, we show model numbers from 1 to 4, ordering the models in the following way: *U5*, *U9*, *U11* and *U13*, respectively.

The mass of the cloudlets for models *U5*, *U9* and *U13* are shown in the top left-hand panel, so that the mass ranges from  $\log(M_f/M_\odot) = 3.6$  to 3.8. Two cloudlets of model *U11* have the largest masses, around  $\log(M_f/M_\odot) = 4.6$ .

In contrast to what we have observed when compared to other physical properties of models *U* with *Ub*, the behavior is different, in the case of the mass of the cloudlets, without any trend.

The mass of the cloudlets for model *Ur* is shown in the top right-hand panel of Fig.14. We see that the models *Ur5*, *Ur9* and *Ur11* all have similar cloudlet masses, which are around  $\log(M_f/M_\odot) = 4.5$ . Meanwhile, the cloudlet mass for model *Ur13* is a little smaller mass than the mass of the other models,  $\approx \log(M_f/M_\odot) = 4.4$ .

Given that models *Urb* have the highest in-fall radial velocity of the all the models, as can be seen in 12, then their mass accretion rate must be the highest too; for this, the mass enclosed is systematically higher than in the other models, although there is not much difference in the mass values observed in the panels of Fig.14 when compared to the big difference in the in-fall radial velocity.

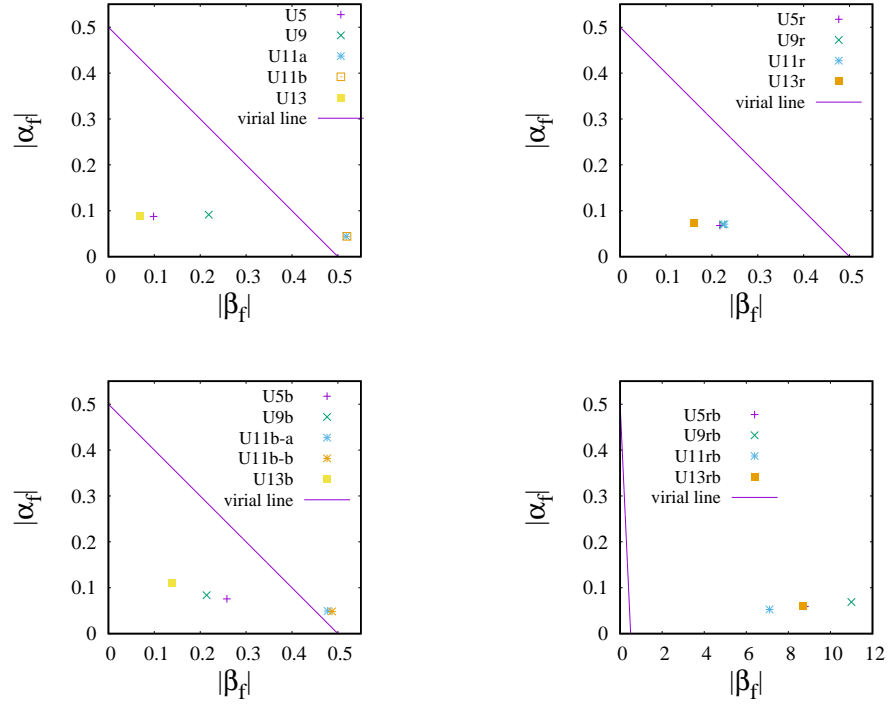


Fig. 13. The ratio of the thermal energy to the gravitational energy  $\alpha$  versus the ratio of the kinetic energy to the gravitational energy  $\beta$ , of the cloudlets defined in Section 4.3, at the same time that the snapshots shown in Fig.4, Fig.5, Fig.6 and Fig.7, respectively. (top left-hand)  $U$  with a low level of turbulence; (top right-hand)  $U_r$  with a low azimuthal velocity; (bottom left-hand)  $U_b$  with a high level of turbulence and (bottom right-hand)  $U_{rb}$  with a high azimuthal velocity.

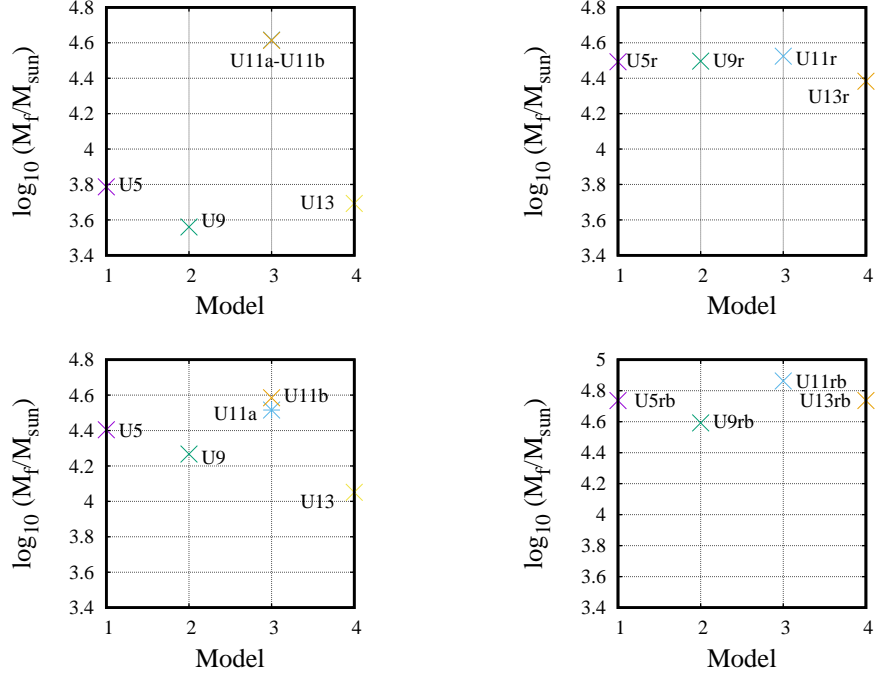


Fig. 14. The log of the mass of the cloudlets defined in Section 4.3, at the same time that the snapshots shown in Fig.4, Fig. 5, Fig.6 and Fig.7, respectively. (top left-hand)  $U$  with a low level of turbulence; (top right-hand)  $Ur$  with a low azimuthal velocity; (bottom left-hand)  $Ub$  with a high of turbulence and (bottom right-hand)  $Urb$  with a high level of turbulence.

It must be emphasized that the mass scale shown in Fig.14 is in agreement with the mass observed for an open cluster of stars, which is around  $10^4 M_{\odot}$ , while the mass scale of a globular cluster of stars is around  $10^5 M_{\odot}$ , see Kumai et al. (1993).

The results of the collapse of a gas core (e.g., in the so called "the standard isothermal simulation") are identified as protostars (Boss (1995), Boss et al. (2000), Burkert and Alves (2009) and Arreaga (2007)). In the same sense, the gas structures obtained from the simulations of the present paper and whose properties are shown in Section 4 can be called a proto-cluster of protostars. As is well-known for simulations of the collapse of a gas core, the mass of the proto-stars depends on the mass of the parent cloud, see for instance Arreaga (2016). The same is expected to be true for proto-clusters.

Finally, it must be recalled that the results displayed in Fig.13 and Fig.14 are taken when

the collapse is still ongoing, so that the peak density is around  $\log(\rho_{\max}/\rho_0) \approx 5$ . As we have seen in Section 3.1, the final state of the collapse reached a peak density around  $\log(\rho_{\max}/\rho_0) \approx 8$ .

## 5. DISCUSSION

Although the dynamics of an isolated turbulent cloud is well-known- see for instance, Goodwin et al. (2004a), Goodwin et al. (2004b) and Goodwin et al. (2006), in Section 5.1- we begin by describing the evolution of the isolated turbulent cloud, to discuss its influence on the collision models considered in Sections 5.2, 5.3 and 5.4. After this, we then commence the discussion about the most important features of the collision models presented in Section 3.

### 5.1. *The collapse of the isolated turbulent cloud*

We mentioned in Sections 1 and 2.2 that the initial conditions of the isolated cloud are chosen to favor its gravitational collapse. The curve of the peak density for the isolated cloud develops a small peak at a time smaller than  $t/t_{ff} = 0.1$ . This increase of density happens because of the multitude of gas lumps formed by the collisions between gas particles that occur simultaneously throughout the cloud. This density peak does not appear for low levels of initial kinetic energies, which is measured by the  $\beta$  ratio defined in Eq.5; for high values of the  $\beta$  ratio, this early peak is quite noticeable.

In contrast, the time required by the isolated cloud to reach the highest density values, for instance  $\log(\rho_{\max}/\rho_0) \approx 6$ , does not depend significantly on the level of the initial energy, at least for a wide range of the initial  $\beta$  ratio. This is due to the fact that almost all of the kinetic energy available is equally dissipated by means of the random collision of particles, as described in the previous paragraph. The time required by the cloud to reach its highest peak density is around  $t/t_{ff} = 2.5$ , which is of the same order of time that can be seen in Fig.3 for the collapse of the collision models.

In the time interval between  $0.1 < t/t_{ff} < 2.0$ , a relaxation of the small gas lumps occurs throughout the cloud, so that the peak density curve decreases quickly. From there, it increases very slowly, up to times  $t/t_{ff} > 2.0$ , in which the final collapse takes place very quickly.

From the point of view of the column density plots, the occurrence of collisions between gas particles, as a consequence of turbulent velocity field implemented initially, is seen as a random formation of many over-dense lumps of gas, which are homogeneously distributed across the entire

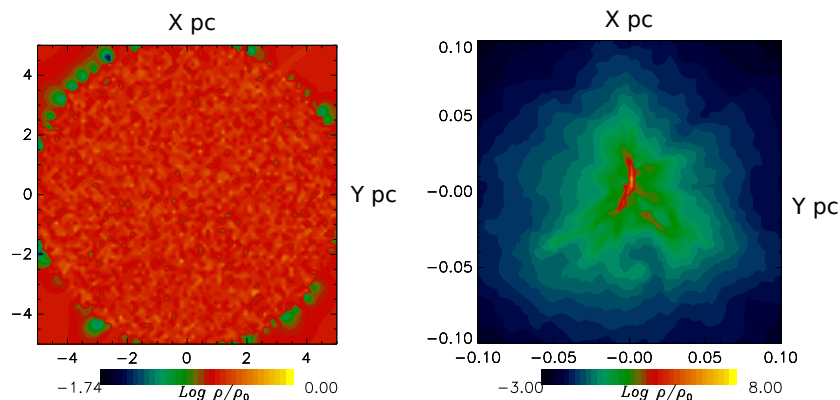


Fig. 15. Column density plots of the isolated turbulent cloud, for a thin slice of gas parallel to the x-y plane. The unit of length is one parsec. The plots are shown in panels as follows: (left-hand) at time  $t/t_{ff} = 0.02$  and peak density  $\log(\rho_{\max}/\rho_0) = 0.53$ ; (right-hand) at time  $t/t_{ff} = 2.5$  and peak density  $\log(\rho_{\max}/\rho_0) = 8.0$ .

cloud volume, see the left-hand panel of Figure 15. Later, when the initial kinetic energy of the cloud is dissipated, the cloud gets a physical state similar to a free-fall collapse, which is seen as a clear tendency to a global collapse towards its central region. However, at the final evolution stage that could be followed in this paper, the mass accretion with spherical symmetry is lost, so that a central dense filamentary structure forms that is highly anisotropic and with a high possibility of fragmenting, see right-hand panel of Figure 15. The behavior described in this section is paradigmatic of turbulence.

### 5.2. Does the turbulence make a difference in the collision simulations ?

The occurrence of the collision between the sub-clouds induced by the translation velocity  $v_L : v_R$  prevents the gas particles from forming small lumps of gas throughout the cloud by means of early random collisions; as explained in the previous Section 5.1.

There is over-dense gas in the contact region between the colliding sub-clouds. This over-density accelerates the collapse of the remaining gas of the cloud, so that the turbulence does not have time enough to get relaxed by dissipation of the kinetic energy. For this reason, the turbulence does not play a fundamental role in the outcome of the simulations, such as  $U$  and  $Ub$ . In fact, if one turns off the turbulence and keeps only the collision process of the sub-clouds in these models, then the results are basically the same.

### 5.3. *Does the level of turbulence make a difference in the collision simulations ?*

We recall that the level of turbulence in the simulations can be modified by introducing an arbitrary multiplicative constant in Eq.1. As we mentioned in Section 2.2.1, there is interest in considering models of turbulent clouds with extreme initial kinetic energy in addition to those clouds with low-level of turbulence, which are more favored statistically. Consequently, we have studied the effect of the level of turbulence on the simulations (i.e., models  $Ub$ ), as can be seen in Table 1.

The average Mach velocity  $\mathcal{M}_p$  of the gas particles for the low-level of turbulence models  $U$  is around  $\mathcal{M}_p \approx 2.9$ . For the radial component of the velocity (calculated with respect to the origin of coordinates of the simulation box), the average Mach number is  $\mathcal{M}_r \approx -0.13$ . For the tangential component of the velocity, the average Mach number is  $\mathcal{M}_t \approx 0.01$ . In the meantime, the translational velocities (around 15 km/s) given to the particles that are to collide are of order  $\mathcal{M}_c \approx 6.6$ . Then, for models  $U$ ,  $\mathcal{M}_c \gg \mathcal{M}_{p,r,t}$ .

For the high-level of turbulence models  $Ub$ , we have an average  $\mathcal{M}_p \approx 25$ . Despite this significant increase of the magnitude of the velocity, the average radial and tangential components do not change appreciably with respect to those of models  $U$ ; that is,  $\mathcal{M}_r \approx -0.12$  and  $\mathcal{M}_t \approx 0.01$ . In contrast, for models  $Ub$  we have  $\mathcal{M}_c \ll \mathcal{M}_p$ .

In spite of this opposite features in the relation of Mach numbers for models  $U$  and  $Ub$  with respect to the translational velocity, the outcome of the simulations  $U$  and  $Ub$  do not show any significant difference with respect to the final configuration of models  $U5$ ,  $U9$  and  $U13$ . The only differences that can be observed are: (i) that the double bridge of gas formed in model  $U11$  becomes only one bridge in model  $U11b$ ; and (ii) that the density peak curves, shown in Fig.3, for the  $Ub$  models are displaced to right-hand side at large free-fall times, so that the collapse takes a little longer than for models  $U$ .

### 5.4. *How useful is the approximation of an azimuthal velocity to mimic tidal forces in the collision simulations ?*

There is an obvious problem with the approximation of a velocity instead of a tidal force, as described in Section 2.3, which is that the azimuthal velocity entered only once in the simulations, as an initial condition of the gas particles. Obviously, this is a severe limitation of the model, similar to that of the turbulence, which is not replenished continually during a simulation. Therefore, the effect of the tidal interaction must be activated during all the simulation time.



However, we observe in Fig. 6 that the immediate effect of the azimuthal velocity on the simulated cloud is a strong tendency for the gas to be accumulated quickly at the cloud's center. In this case, if the azimuthal velocity terms given in Eq. 10 were implemented at every time step of the simulation, then to model more appropriately the tidal force at all the simulation time one would expect this tendency to accelerate the central collapse of the cloud.

It should be emphasized that the previous statement is based on the results of a very naive model, in which the only information about the massive center exerting a gravitational force on the cloud, is by means of the circular velocity, which is given by  $\sqrt{2GM(R)/R}$ , as described in Section 2.3.

According to Section 2.3, the approximation of the azimuthal velocity is valid as long as the ratio between the cloud radius to the distance to the gravitational center is quite small. A way to check the applicability of this approximation is obviously to make the calculation without the approximation. However, this is not an immediate calculation. The main difficulty is the difference in length and mass scales when considering a small cloud (with a very few parsecs of radius) near a massive object (probably with a scale of kpc in radius, separated from the cloud by several hundreds of pc or even a kpc and whose mass can quite greater than that of the cloud), both of which must have evolved together in the same simulation code.

For instance, Gnedin (2003) resorts to a re-simulation technique, so that a low-resolution simulation of the massive object (e.g., a central dwarf galaxy) is first simulated to obtain an approximate gravitational potential. This is then used in a second high-resolution simulation of the cloud, in which this potential is taken into account as an external time-varying field on the gas particles. However, applying this technique to the problem presented in this work would require a future paper.

### 5.5. *A brief review of the literature on this subject*

A lot of papers have simulated isolated clouds and followed their collisions. However, simulations of clouds under the influence of an external gravitational potential are limited in number.

Let us now mention briefly some results of more accurate calculation methods of the tidal effects on clouds, which is a subject that has a long history. For instance, Sigalotti and Klapp (1992) used a time-varying gravitational potential to calculate the equal-sized cloud-cloud tidal

interaction of clouds that are in an elliptic orbit, and reported configuration transformations on the clouds in their course to collapse.

More recently, Longmore et al. (2013) proposed that the collapse of the Brick is a progenitor of a star cluster, whose collapse was triggered as a consequence of the tidal compression exerted by Sgr B2 during the most recent peri-center passage of the Brick.

Kruijssen et al. (2015) determined a realistic orbit of a dense gas streams in the CMZ. In a subsequent paper, Kruijssen et al. (2019) calculated the tidal interaction of the galactic center on the orbit followed by the dense gas streams of the CMZ. They found that the tidal interaction acting upon the clouds makes a compression on the vertical direction, which causes the clouds to become pancake-like structures.

Later, Dale et al. (2019) simulated the evolution of turbulent clouds in orbit at the CMZ. The authors were prepared to have similar magnitude of the kinetic energy to the gravitational energy and found that the clouds collapse rapidly. This paper is a mature way of simulating tidal force in cloud dynamic evolutions by introducing the tidal force potential.

#### 5.6. *Applicability of these simulations to represent the evolved clouds of the CMZ*

In view of Sections 5.2 and 5.3, the collision process (and its parameters) is clearly the dominant physical mechanism in shaping the appearance of the cloud in the simulation outcome. It is possible that this collision of sub-clouds and with the cloud's self-gravity, are the dominant processes of the cloud evolution, even over the tidal interaction with the massive center, and above all, for the small scale of the circular velocity that is induced, as compared to the magnitude of the other velocities involved, which are the turbulent and the translational velocities, see Section 2.3.

For models  $U5$ ,  $U9$ , and  $U13$ , the geometry of the resulting configuration can be well characterized by defining a center and a radius of a cloudlet. For model  $U11$ , this spherical structure does not make sense, as can be seen in Figs. 4 and 8. The outcome of model  $U11$  is a complex, structured molecular gas cloud that exhibits an interconnected network of components. This is the only model that can be compared or approximated to the cloud configuration called the Brick.

In fact, for the Brick, a shell-like structure with radius of 1.3 pc has been revealed from observations in the integrated intensity map of SO. For instance, see Figs.1 and 3 of Longmore et al. (2012); Figs.1 and 3 of Kauffmann et al. (2013); Figs. 1 and 2 of Higuchi et al. (2014). Kruijssen et al. (2019) presented three panels in their Figure 6, to compare the results of ALMA observations of the

Brick to a synthetic observations obtained from a numerical simulation. A complex gas structure can be seen in these panels, in which the gas condenses in a persistent diagonal direction with many twisted and bending filaments connected in a messy way. Model *U11* of this paper clearly shows a similar diagonal direction of the dense gas.

It may seem that there is a huge problem with models *Ur*, given that all of the different structures obtained as a result of the collision process in model *U* are destroyed because of the azimuthal velocity of models *Ur*. However, the configuration obtained in these models *Ur* can be well recognized as the final outcome of the formation process of a YMC, which are observed to be a strongly centrally condensation of gas, with a mass enclosed of stars about  $10^4 M_{\odot}$  in a size of one pc, see for instance Rathborne et al. (2015). The Arches cloud is an example of this kind of observed configuration, see Portegies al. (2010).

## 6. CONCLUDING REMARKS

We examined models with three kinds of velocities, which are turbulent, translational and azimuthal. These velocity kinds were introduced as initial conditions of the simulation particles. Then, the particles are left to evolve as a self-gravitating gas by using the public hydrodynamic code Gadget2.

The role played by these velocities determines the subsequent evolution of the cloud. It must be emphasized that all of the models that are considered in this paper include the same turbulent velocity spectrum (calibrated to fix the initial energies and physical properties which favors the global collapse of the cloud) and the same translational velocity (which produces the collision between two dissimilar sub-clouds).

In models *U* with a low level of turbulence, we observed the coalescence of the sub-clouds, enriched by the asymmetry in radii and translational velocities of the sub-clouds. When the impact parameter was introduced, the model produced a binary system with interconnected arms and with a complex structure. In models *Ub*, with a high level of turbulence, we obtained a similar structure to that observed in models *U*. However, in model *Ub*, the arms and tails are larger than those of models *U*. The most significant change between these simulations was observed in models *U11* and *U11b*, such that the double bridge of gas found in model *U11* becomes a single bridge in model *U11b*.

The free parameters of these models *U* and *Ub* (i.e., the impact parameter, the radii and the translational velocities of the sub-clouds) have been kept fixed. If these parameters were

allowed to vary, then it will certainly produce more interesting configuration outcomes.

In addition to the turbulent and the translational velocities, the last models,  $Ur$  and  $Urb$ , also include a low and high azimuthal velocity, respectively. The purpose of this azimuthal velocity was to mimic, at least initially, the effect of the tidal force on the cloud. The magnitude of the azimuthal velocity induced in the cloud depends explicitly on the distance  $R$  from the cloud and the mass  $M$  of the gravitational center by means of the circular velocity  $\sqrt{2GM(R)/R}$ .

We observed that the presence of this azimuthal velocity in the simulation always induces a centrally located lump of gas in the cloud. If  $V_{\text{cir}}$  is small, then the collision process of the sub-clouds dominates the dynamics of the cloud, even over the turbulence and therefore the cloud evolution changes little of the that observed without the azimuthal velocity. However, if  $V_{\text{cir}}$  is large compared with the other velocities involved, then the cloud evolution changes significantly: reducing too much the collapsing time, suppressing any sign of the collision of the sub-clouds, and producing a central condensation, so that the different structures obtained as a result of the collision process are destroyed. In fact, we observed that the cloud collapses faster when the azimuthal velocity is larger.

We recall that this approximation is only valid when the ratio between the cloud radius to the distance to the gravitational center is quite small; in other words, only for spatially compact clouds. For this kind of cloud, the observation described above is in good agreement with the known fact that clouds in the CMZ are observed to be denser than clouds in the ISM. Furthermore, because gravity is a ubiquitous force, this azimuthal velocity approximation allows us to explain why centrally condensed clouds are more abundant than uniform clouds in the ISM, see Ward-Thompson (1994) and André et al. (1998).

In addition to information on shapes, we have also provided information about the physical properties of the final collapse products and their surrounding region, which include the density, mass and velocity profile. As mentioned in Section 5.6, we have found proto-cluster structures that are still in their formation process. Furthermore, by the mass scale and the radius of the resulting centrally condensed configurations, the outcomes of models  $Ur$  and  $Urb$  can be identified with the final process of the formation of a young massive proto-cluster. Basically, the models show a strong flow of particles towards the cloud center, at different radial velocities ( a few Mach ) and with some bending trajectories.

The authors gratefully acknowledges the computer resources, technical expertise, and

support provided by the Laboratorio Nacional de Supercómputo del Sureste de México through grant number 202201010N.

## REFERENCES

- Anathpindika, S. 2009a, *A&A*, 504, 437.
- Anathpindika, S. 2009b, *A&A*, 504, pp.451-460.
- Anathpindika, S. 2010, *MNRAS*, 405, pp.1431-1443.
- André, P., Bacmann, A., Motte, F. and Ward-Thompson, D., 1998, in *The Physics and Chemistry of the Interstellar Medium*, ed. V. Ossenkopf, J. Stutzki and G. Winnewisser (Zermatt: GCA-Verlag), 241.
- Arreaga-García, G., 2007, *ApJ*, 666, pp. 290-308.
- Arreaga-García, G., 2016, *Revista Mexicana de Astronomía y Astrofísica*, 52, pp. 155-169.
- Arreaga-García, G., 2017, *Revista Mexicana de Astronomía y Astrofísica*, 53, pp. 361-384.
- Arreaga-García, G., 2018, *Astrophysics and Space Science*, 363, pp. 157-169.
- Balsara, D., 1995, *J. Comput. Phys.*, 121, 357.
- Ballesteros-Paredes, J., Vázquez-Semadeni, E., Palau, A. and Klessen, R.S., 2018, *MNRAS*, 479, p.2112-2125.
- Bally J., Stark A. A., Wilson R. W. and Henkel C., 1988, *ApJ*, 324, 223.
- Bate, M.R. and Burkert, A., 1997, *MNRAS*, 288, 1060.
- Bekki, K. and Couch, W. J., 2004, *ApJ*, 602, pp. 730-737.
- Bergin, E. and Tafalla, M., 2007, *Annu. Rev. Astro. Astrophys.*, 45, 339.
- Bolatto A., Leroy A., Roslowsky E., Walter F., Blitz L., 2008, *ApJ*, 686, 948.
- Boss, A.P., 1995, *ApJ*, 439, pp.224-236.
- Boss, A.P., Fisher, R.T., Klein, R. and McKee, C.F., 2000, *ApJ*, 528, 325.
- Burkert, A. and Alves, J. 2009, *ApJ*, 695, 1308.
- Caselli, P., Benson, P. J., Myers, P. C. and Tafalla, M., 2002, *ApJ*, 572, pp.238-263.
- Churchwell, E., Povich, M.S., Allen, D., et al. 2006, *ApJ*, 649, 759.
- Dale, J.E., I. A. Bonnell, I.A. and Whitworth, A.P., 2007, *MNRAS*, 375, pp. 1291-1298.
- Dale, J.E., Kruijssen, J.M.D and Longmore, S.N., 2019, *MNRAS*, 486, pp. 3307-3326.
- Dobbs, C.L., Bonnell, I.A. and Clark, P.C., 2005, *MNRAS*, 360, pp. 2-8.
- N. Furukawa, N., Dawson, J.R., A. Ohama, A., Kawamura, A., Mizuno, N., Onishi, T. and Fukui, Y., 2009, *ApJ*, 696, pp.L115-L119.
- Gnedin, O.Y., 2003, *ApJ*, 582, pp.141-161.
- Goodwin, S.P., Whitworth, A.P. and Ward-Thompson, D., 2004a, *A&A*, 414, pp.633-650.
- Goodwin, S.P., Whitworth, A.P. and Ward-Thompson, D., 2004b, *A&A*, 423, pp.169-182.

- Goodwin, S.P., Whitworth, A.P. and Ward-Thompson, D., 2006, *A&A*, 452, pp. 487-492.
- Gomez, G.C., Vazquez-Semanedi, E., Shadmehri, M. and Ballesteros-Paredes, J., 2007, *ApJ*, 669, pp. 1042-1049.
- Guerrero-Gamboa, R. and Vázquez-Semadeni, E., 2020, arXiv:2009.04676v1, astro-ph.GA.
- Habe, A., and Ohta, K. 1992, *PASJ*, 44, 203.
- Hachisu, I. and Heriguchi, Y., 1984, *Astron. Astrophys.*, 140, 259.
- Hachisu, I. and Heriguchi, Y., 1985, *Astron. Astrophys.*, 143, 355.
- Hausman, M.A. 1978, *ApJ*, 245, 72.
- Higuchi, A.E., Chibueze, J.O., Habe, A., Takahira, K. and Takano, S., 2014, *ApJ*, 147, pp.141-148.
- Hillenbrand, L. A. and Hartmann, L. W., 1998, *ApJ*, 492, pp.540-.
- Jackson, J.M., Contreras, Y., Rathborne, J.M., Whitaker, J.S., Guzmán, A., Stephens, I.W., Sanhueza, P., Longmore, S., Zhang, Q. and Allingham, D., 2018, *ApJ*, 869, pp.102-114.
- Jijina, J., Myers, P.C. and Adams, C., 1999, *ApJ*, SUPPLEMENT SERIES, 125, pp.161-236.
- Kauffmann, S., Pillai, T. and Goldsmith, P.F., 2013, *ApJ*, 779, 185.
- Kimura, T. and Tosa, M. 1996, *A&A*, 308, 979.
- Kirk, H., Offner, S.S.R and Redmond, K.J., 2014, *MNRAS*, 439, pp.1765-1780.
- Kitsionas, S. and Whitworth, A.P., 2007, *MNRAS*, 378, pp. 507-524.
- Klein, R.I. and Woods, D.T. 1998, *ApJ*, 497, 777.
- Kruijssen, J. M. D., Dale, J.E. and Longmore, S.N., 2015, *MNRAS*, 447, pp.1059-1079.
- Kruijssen, J. M. D., Dale, L. M. D., Longmore, S.N., Walker, D.L., Henshaw, J.D., Jeffreson, S. M. R., Petkova, M. A., Ginsburg, A., Barnes, A. T., Battersby, C. D., Immer, K., Jackson, J. M., Keto, E. R., Krieger, N., Mills, E.A.C., Sánchez-Monge, A., Schmiedeke, A., T. Suri S. T. and Zhang, Q., 2019, *MNRAS*, 484, pp. 5734-5754.
- Kumai, Y., Basu, B. and Fujimoto, M., 1993, *ApJ*, 404, pp. 144-161.
- Lattanzio, J.C., Monaghan, J.J., Pongracic, H. and Schwarz, M.P. 1985, *MNRAS*, 215, 125.
- Lis, D.C. and Menten, K.M., 1998, *ApJ*, 507, pp.794-804.
- Longmore, S.N., Rathborne, J., Bastian, N., Alves, J., Ascenso, J., Bally, J., Testi, L., Longmore, A., Battersby, C., Bressert, E., Purcell, C., Walsh, A., Jackson, J., Foster, J., Molinari, S., Meingast, S., Amorim, A., Lima, J., Marques, R., Moitinho, A., Pinhao, J., J. Rebordao, J. and Santos, F.D., (2012), *ApJ*, 746, pp.117-127.
- Longmore, S. N., Bally, J., Testi, L., Purcell, C. R., Walsh, A. J., Bressert, E., Pestalozzi, M., Molinari, S., Ott, J., Cortese, L., Battersby, C., Murray, N., Lee, E., Kruijssen, J. M. D., Schisano, E. and Elia, D., 2013, *MNRAS*, 429, pp. 987-1004.
- Longmore, S. N., Kruijssen, J. M. D., Bally, J., Ott, J., Testi, L., Rathborne, J., Bastian, N., Bressert, E.,

- Molinari, S., Battersby, C. and Walsh, A. J., 2013, MNRAS, 433, pp. L15-L19.
- Launhardt, R., Zylka, R. and Mezger, P.G., 2002, A&A, 384, pp. 112-139.
- Marinho, E.P. and Lepine, J.R.D., 2000, A&A Suppl., 142, 165.
- Mills, E.A.C, 2017, arXiv, astro-ph.GA., 1705.05332v1.
- Miyama, S.M., Hayashi, C. and Narita, S., 1984, ApJ, 279, 621.
- Molinari, S., Bally, J., Noriega-Crespo, A., Compiègne, M., Bernard, J.P., Paradis, D., Martin, P., Testi, L., Barlow, M., Moore, T., Plume, R., Swinyard, B., Zavagno, A., Calzoletti, L., Giorgio, A.M.D., Elia, D., Faustini, F., Natoli, P., Pestalozzi, M., Pezzuto, S., Piacentini, F., Polenta, G., Polychroni, D., Schisano, E., Traficante, A., Veneziani, M., Battersby, C., Burton, M., Carey, S., Fukui, Y., Li, J.Z., Lord, S.D., Morgan, L., Motte, F., Schuller, F., Stringfellow, G.S., Tan, J.C., Thompson, M.A., Ward-Thompson, D., White, G. and Umana, G., 2011, ApJL, 735, pp. L33-L40.
- Petkova, M.A., Kruijssen, J.M.D, Kluge, A.L., Glover, S.C.O, Walker, D.L., Longmore, S.N., Henshaw, J.D., Reissl, S. and Dale, J.E., (2021), arXiv, 2104.09558.
- Portegies Zwart, S. F., McMillan, S. L. W. and Gieles, M. 2010, ARAA, 48, pp. 431.
- Rathborne, J. M., Longmore, S. N., Jackson, J. M., Alves, J. F., Bally, J., Bastian, N., Contreras, Y., Foster, J. B., Garay, G., Kruijssen, J. M. D., Testi, L. and Walsh, A.J., 2015, ApJ, 802, pp.125-145.
- Roslowky E., Engargiola G., Plambeck R., Blitz L., 2003, ApJ, 599, 258.
- Scoville, N.Z., Sanders, D.B. and Clemens, D.P., 1986, ApJ, 310, pp.L77-L81.
- Sigalotti, L.D., and Klapp, J., 1992, MNRAS, 254, pp.111-131.
- Springel, V., 2005, MNRAS, 364, 1105.
- Tafalla M., Mardones D., Myers P. C., Caselli P., Bachiller R. and Benson P. J., 1998, ApJ, 504, 900.
- Takahira, K., Tasker, E.J., and Habe, A. 2014, ApJ, 792, 63.
- Testi, L., Anneila, I.S., Luca, O., and Onello, J.S. 2000, ApJ, 540, L53.
- Torii, K., Enokiya, R., Sano, H., et al. 2011, ApJ, 738, 46.
- Truelove, J.K., Klein, R.I., McKee, C.F., Holliman, J.H., Howell, L.H. and Greenough, J.A., 1997, ApJ, 489, L179.
- Vazquez-Semanedi, E., Gomez, G.C., Jappsen, A.K., Ballesteros-Paredes, J., Gonzalez, R. and Klessen, R.S., 2007, ApJ, 657, pp. 870-883.
- Ward-Thompson, D., Scott, P. F., Hills, R. E. and André, P. 1994, MNRAS, 268, pp.276-.
- Yamada, R.I., Fukui, Y., Sano, H., Tachihara, K., Bieging, J.H., Enokiya, R., Nishimura, A., Fujita, S., Kohno, M. and Tsuge, K., arXiv:2106.01852.

Guillermo Arreaga-García: Departamento de Investigación en Física  
Universidad de Sonora.  
Apdo. Postal 14740, C.P. 83000, Hermosillo, Sonora, Mexico.  
guillermo.arreaga@unison.mx